



Dynamics of Fluorescent Imaging for Rapid Tear Thinning

L. Zhong¹  · R. J. Braun¹ · C. G. Begley² · P. E. King-Smith³

Received: 16 April 2018 / Accepted: 27 September 2018 / Published online: 15 October 2018
© Society for Mathematical Biology 2018

Abstract

A previous mathematical model has successfully simulated the rapid tear thinning caused by glob (thicker lipid) in the lipid layer. It captured a fast spreading of polar lipid and a corresponding strong tangential flow in the aqueous layer. With the simulated strong tangential flow, we now extend the model by adding equations for conservation of solutes, for osmolarity and fluorescein, in order to study their dynamics. We then compare our computed results for the resulting intensity distribution with fluorescence experiments on the tear film. We conclude that in rapid thinning, the fluorescent intensity can linearly approximate the tear film thickness well, when the initial fluorescein concentration is small. Thus, a dilute fluorescein is recommended for visualizing the rapid tear thinning during fluorescent imaging.

Keywords Tear film · Marangoni effect · Dry eye · Fluorescent imaging

1 Introduction

Millions of people seek eye care for dry eye syndrome (DES) (Stapleton et al. 2015). Its symptoms include blurred vision, a gritty or dry sensation, as well as other discomfort, and thus diminish quality of life (Mertzanis et al. 2005; Miljanović et al. 2007). The prevalence of DES is estimated ranging from 5 to 50% under different diagnostic criteria in different regions (Nelson et al. 2017). Further understanding of DES is needed to improve treatments for this common condition.

One of the core mechanisms of DES is tear film instability or tear breakup (TBU), which causes the tears to disrupt quickly and thus poorly coat the surface of the eye (Lemp et al. 2007; Craig et al. 2017). The tear film is a multilayered film. It is composed of a very thin lipid layer on its anterior surface over a relatively thick

✉ L. Zhong
lanzhong@udel.edu

¹ Department of Mathematical Sciences, University of Delaware, Newark, DE 19716, USA

² School of Optometry, Indiana University, Bloomington, IN 47405, USA

³ College of Optometry, The Ohio State University, Columbus, OH 43218, USA

aqueous layer with a bound mucin layer (glycocalyx) at the posterior side (the ocular surface). The aqueous layer is largely water (Holly 1973) and is normally treated as a Newtonian fluid that is close to water in its properties (Wong et al. 1996; Sharma 1998; Miller et al. 2002; Braun and Fitt 2003; Braun 2012). The aqueous layer contains ions from salts and a number of large proteins and mucins (Bron et al. 2004); the large molecules cause slightly shear thinning properties of the tear film (Nagyová and Tiffany 1999). The glycocalyx consists of glycosylated proteins that help make the ocular surface wettable, and it is thought to have important lubrication (Pult et al. 2015) and protective functions (Gipson 2004; Govindarajan and Gipson 2010; Bron et al. 2015). A damaged glycocalyx has been hypothesized to promote TBU and tear film instability (Sharma and Ruckenstein 1985; Gipson 2004; Yokoi and Georgiev 2013b; Yanez-Soto et al. 2014; Yokoi et al. 2017). The lipid layer is primarily composed of nonpolar lipids on the order of tens of nanometers thick (Norm 1979; King-Smith et al. 2011). At the lipid/aqueous interface, there are surface-active polar lipids and other surface-active molecules. The nonpolar lipid layer is generally, though perhaps not universally, believed to be a barrier to evaporation due to the nonpolar components (Mishima and Maurice 1961; King-Smith et al. 2010; Paananen et al. 2014). The polar lipids act as a surfactant which can drive flow in the aqueous layer (Johnson and Murphy 2004; McCulley and Shine 1997). Differences in lipid layer structure may correlate with DES. Experimental approaches include: specular reflection with keeler tearscope (Craig and Tomlinson 1997); high-resolution microscopy (King-Smith et al. 2011); X-ray scattering methods (Leiske et al. 2012; Rosenfeld et al. 2013).

The Dry Eye Workshop (Craig et al. 2017) has classified DES into three categories, where two of them are predominant: aqueous tear-deficient dry eye (ADDE) and evaporative dry eye (EDE). The third category is non-mutually exclusive; a mixture of ADDE and EDE. The core mechanisms of DES are generally accepted to be tear hyperosmolarity and tear film instability (Lemp et al. 2007). Tear hyperosmolarity may result from either water evaporation or deficiency of tear generation (Lemp 2007; Braun et al. 2015). Hyperosmolarity in the tear film can generate stress on the ocular surface and can cause inflammation and eventually ocular surface damage (Li et al. 2006). Tear osmolarity has been proposed as the standard (Farris 1994; Lemp et al. 2011) for a DES test due to the fact that a dry eye is linked to hyperosmolarity (Tomlinson et al. 2006).

Osmolarity is defined as a combined concentration of osmotically active solutes, primarily salt ions in the aqueous layer (Stahl et al. 2012). When an osmotic difference exists between the tear film and corneal epithelium, and osmotic flow is generated which is typically from the cornea to the tear film (Peng et al. 2014; Braun et al. 2015). Osmolarity is typically difficult to measure in the tear film. Older methods require either a complicated procedure or a large sample size of tears (Gilbard et al. 1978; Farris 1994). Recently, lab-on-a-chip technology has enabled a noninvasive and quick test that measures osmolarity in a 50-nL tear sample from the inferior meniscus (Lemp et al. 2011). This technology is able to measure osmolarity with high precision and accuracy (Versura and Campos 2013). However, work remains to be done to correlate tear film osmolarity with signs and symptoms of DES (Messmer et al. 2010; Szalai et al. 2012; Amparo et al. 2014; Sebbag et al. 2017).

Water fluxes in the tear film during the interblink may be evaporative, osmotic and/or tangential (King-Smith et al. 2008). Water is typically lost from the tear film to the air outside the eye due to evaporation (Nichols et al. 2005). Water may be supplied to the tear film via an osmotic flux by osmolarity differences across the tear/corneal interface. Tangential flow is along the corneal surface, and it can be driven by: (i) capillarity, which are pressure differences due to surface tension and curvature of the tear/air interface (Oron et al. 1997); (ii) the Marangoni effect, where surface concentration differences generate shear stresses on the tear/air interface (Craster and Matar 2009); and (iii) intermolecular forces like van der Waals forces (Winter et al. 2010; Zhang et al. 2004). Based on the direction of the tangential flow, it can be classified as either convergent, which flows toward TBU and slows down the thinning, or divergent, which flows away from TBU and promotes thinning. For an axisymmetric spot, convergent flow would be radially inward, and divergent flow would radially outward. Evaporative, osmotic and tangential flows can all contribute to TBU, although they may be on different timescales; this is discussed further below.

There are many different imaging methods to observe the dynamics of tears and TBU. King-Smith et al. (2018) recently reviewed five different imaging systems: (i) fluorescence for tear volume, (ii) reflection for tear film surface, (iii) interferometry for the thickness and structure of tear film lipid layer (TFLL), (iv) refraction for the shape of tear film surface, and (v) thermal radiation for temperature distribution. Fluorescence is the most widely used method despite some quantitative uncertainty about absolute thickness measurement; however, when combined with other imaging methods, it is useful for studying the dynamics and mechanism of TBU. For example, when combined with interferometry, aqueous layer dynamics can be correlated with TFLL dynamics to understand how they are intimately linked (King-Smith et al. 2013b). Excessive evaporation can lead to TBU for very thin areas (Nichols et al. 2005; King-Smith et al. 2010) or holes in the TFLL, while the Marangoni effect has been proposed to explain TBU under globs of thick TFLL (King-Smith et al. 2013b). Such combinations of simultaneous imaging, particularly including the TFLL, can help us determine the mechanisms of TBU more precisely (Braun et al. 2015). Strong correlation between fluorescence and thermal imaging has been observed, which supports the conclusion that evaporation is a non-negligible cause of TBU in many cases (Kamao et al. 2011; Su et al. 2014).

Fluorescein and other dyes have been used in a variety of ways, including: assessment of the condition of the ocular surface via staining of epithelial cells (Efron 2013; Bron et al. 2015); estimation of tear drainage rates or turnover times (Webber and Jones 1986); visualization of overall tear film dynamics (Benedetto et al. 1986; Begley et al. 2013b; King-Smith et al. 2013a; Li et al. 2014); estimation of first breakup times of the tear film (Norn 1969); and the temporal progression of tear film breakup areas (Liu et al. 2006). There are different ways that fluorescence may be used to visualize the tear film. For visualizing the tear film, sodium fluorescein is instilled and both sodium ions dissociate at physiological pH. Under those conditions, the fluorescein glows green when illuminated with blue light. In the dilute regime, the fluorescein concentration is below the critical concentration where maximum intensity green light is emitted for fixed depth of fluid, and the intensity of the fluorescence from the tear film is proportional to its thickness. In the concentrated (or self-quenching) limit above

the fluorescein concentration where maximum intensity occurs, the intensity drops as the tear film thins in response to evaporation, and the thickness is roughly proportional to the square root of the intensity for a spatially uniform (flat) tear film (Nichols et al. 2012; Braun et al. 2014). Mathematical theories are able to capture a number of aspects of the overall tear film flow observed experimentally over the exposed ocular surface (Maki et al. 2010b; Li et al. 2014, 2017). We use the shorthand FL to indicate fluorescence or fluorescein below.

A variety of mathematical models of the tear film have been reviewed recently (Braun 2012; Braun et al. 2015). Most models of tear film are 1D single-layer models, with the common simplifications that consider the aqueous layer to be a Newtonian fluid (Wong et al. 1996; Sharma 1998; Miller et al. 2002; Braun and Fitt 2003), treat the TFLL as an insoluble surfactant monolayer (Berger and Corrsin 1974; Jones et al. 2006; Aydemir et al. 2010), and assume the substrate (corneal surface) under the tear film to be flat impermeable surface (Braun et al. 2012). These simplified models have enabled investigation of important effects on tear dynamics over the open surface of the eye, such as evaporation into the air (Winter et al. 2010), heat transfer within the tear film and outside environment (Scott 1988), van der Waals forces acting on the aqueous layer (Oron and Bankoff 1999; Israelachvili 2011; Zhang et al. 2004), osmosis across the corneal surface (Braun 2012), Marangoni effects induced by varying concentration of polar lipid (Aydemir et al. 2010; Berger and Corrsin 1974), complete blink cycles (Braun and King-Smith 2007; Zubkov et al. 2012), and partial blink cycles (Heryudono et al. 2007). Related 2D models of tear film dynamics have also been developed (Maki et al. 2010a, b; Li et al. 2014, 2017).

In several mathematical models, the lipid layer is simplified to be only polar lipid in an insoluble surfactant monolayer, where the concentration gradient can induce a Marangoni contribution to the flow. An early model of the upward motion of the tear film following a blink in one dimension (1D) was developed by Berger and Corrsin (1974); their predictions regarding upward movement of the tear film have been confirmed by a number of later observations (Owens and Phillips 2001; Jones et al. 2006; King-Smith et al. 2009). Subsequent models incorporating a lipid monolayer were developed in the context of tear film formation during blinking (Jones et al. 2005, 2006; Aydemir et al. 2010) and were able to successfully capture aspects of tear film formation. Adding osmolarity to the model with a polar lipid monolayer was accomplished by Zubkov and coworkers for blinking (Zubkov et al. 2012) and for saccades (Zubkov et al. 2013). Blinking 1D domains that include both a polar lipid monolayer and a floating nonpolar lipid layer have also been developed (Bruna and Breward 2014).

Mathematical models of TBU have included an insoluble polar lipid layer as a surfactant monolayer, but it can also affect evaporation. Some models have focused on evaporation based on the amount of lipid present in the TFLL. Siddique and Braun (2015) built a one-dimensional (1D) evaporative model, where evaporation depends on pressure, temperature, and surfactant concentration. The model successfully captures TBU induced by evaporation, but cannot detect the increased evaporation rate caused by surfactant concentration. Peng et al. (2014) developed another 1D single-layer model, which captures TBU induced by the excessive evaporation due to a spatial variation in the thickness of a stationary lipid layer. The rupture of a hypothesized

mobile precorneal mucus coating of 20–50 nm over the ocular epithelial surface was investigated by Zhang et al. (2004); their results indicated that, for a thin mobile mucus layer, van der Waals forces act significantly to disrupt the mucus layer and the corresponding tear breakup time (TBUT) matches the clinical TBUT for a dry eye and a healthy eye. Recently, Stapf et al. (2017) studied a model with two mobile Newtonian fluid layers, one is an aqueous layer and the other is the lipid layer, that is adapted from the prior model of Bruna and Breward (2014). This model has shown that the Marangoni effect due to lipid defects can reduce the lipid layer thickness, which subsequently allows elevated evaporation and then TBU.

However, none of these models are specially designed to explain the lipid-driven rapid thinning that causes TBU shortly after the blink. Simultaneous imaging of fluorescein and lipid layer thickness shows that dark spots (TBU regions) appear within 4 s and appear to be underneath relative thick areas of lipid, which we call ‘globs’ (King-Smith et al. 2013b). In some observations, TBU occurs much faster, in just tenths of seconds. Different mechanisms for this type of TBU have been proposed: one is divergent tangential flow due to differences in surfactant concentration differences (King-Smith et al. 2008), and another is decreased wettability of the cornea (Sharma and Ruckenstein 1985, 1986; Sharma and Khanna 1998; Yokoi and Georgiev 2013a, b; Yanez-Soto et al. 2015). Tangential flow is the only process likely to be fast enough to account for rapid TBU. Firstly, osmotic flow is too small to slow this rapid thinning (Nichols et al. 2005). Secondly, evaporation is too slow to account for rapid TBU, except possibly in the case of severe ADDE with a very thin tear film. It takes at least 8 s to observe a dark spot for a 3.5 μm aqueous layer with an evaporation rate of 25 $\mu\text{m}/\text{min}$. However, TBUT can be as short as 0.2 s, but the highest observed evaporation rate is 25 $\mu\text{m}/\text{min}$ (King-Smith et al. 2010). Recently, Yokoi and Georgiev (2013a, b) have proposed that dewetting of the ocular surface can explain roughly circular rapid breakup; they propose that an area of highly hydrophobic surface may exist due to a faulty glycocalyx which leads to rapid TBU. Under this assumption, the non-wetted ocular surface should correspond to a fixed location on the epithelial surface for the dark spot after the next blink. Their data appear to show that level of repeatability in some cases. However, our data show that dark spots were observed at different positions in the fluorescence images after each blink (Zhong et al. 2018); this implies that Marangoni-driven tangential flow may provide an explanation for many TBU events with rapid thinning. We suspect that both types of TBU may occur.

Zhong et al. (2018) developed a Marangoni-driven model for rapid TBU that was able to explain a significant part of our experimental observations. In the terminology of Bitton and Lovasik (1998), they used both axisymmetric spot models and linear streak models to test the hypothesis that globs can cause a strong tangential flow which subsequently drives TBU near the glob. In both models, they simulated the globs’ different composition by assuming that the glob has a higher surfactant concentration than the surrounding aqueous/air interface. Increased surfactant concentration lowered the aqueous/air surface tension and thus driving flow via the Marangoni effect. Their lubrication model used scaling appropriate to Marangoni-driven flow, and it captured appropriate length and timescales for rapid TBU in many cases.

In this article, we use mathematical models for spots and streaks to study rapid TBU near a glob when using fluorescence imaging. Like Zhong et al. (2018), we

choose appropriate length and timescales in order to derive nonlinear partial differential equations (PDEs) using lubrication theory (Oron et al. 1997; Craster and Matar 2009). Both models are solved in the local region for the tear film thickness (h); the pressure (p) and solute concentrations for osmolarity (c) and fluorescein (f) inside the tear film; and the insoluble surfactant concentration (Γ) on the tear/air interface. Using reasonable choices for the parameters, TBUT is matched with clinical experiments. We also compute the fluorescent intensity (I) from the tear film in order to determine how the intensity can be used to estimate the thickness during, and the progression of, TBU.

In Sect. 2, we provide sample results from clinical experiments and discuss our assumptions of our model. In Sect. 3, we derive the mathematical models. Corresponding numerical results of both models are shown in Sect. 4. Discussion and conclusions follow; some details are given in the Appendices.

2 Fluorescent Imaging and Mechanisms of TBU

FL imaging is the most frequently and widely used technique in dry eye diagnosis. It can be used for grading ocular surface staining and measuring tear film stability (Wolffsohn et al. 2017). The TBU time obtained using FL imaging is often called the fluorescein breakup time or FBUT. FBUT is the time between the complete blink and the appearance of a sufficiently dark spot in fluorescent images. When measuring FBUT, a small amount of fluorescein is instilled into the subjects' eye using either a micropipette or dye-impregnated strips. Subjects are asked to blink and then hold their eyes open as long as they can.

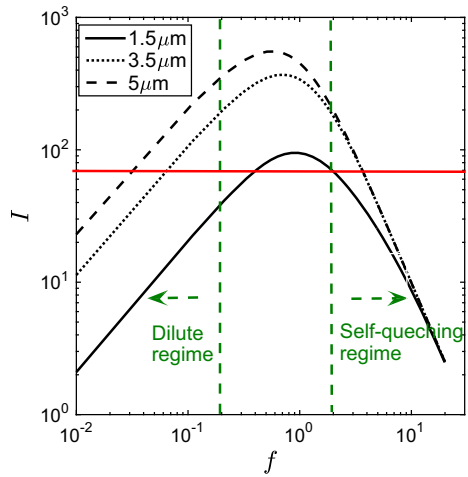
Besides FBUT, the percentage of area of breakup (ABU) can be used as a quantitative technique for tracking the TBU progression. ABU is defined as the ratio of number of pixels inside the TBU region to those in the area of the exposed cornea, which is found to distinguish between control and dry eyes (Liu et al. 2009; Begley et al. 2006, 2013a).

There is agreement that less water is underneath the lipid layer in a TBU region. For the purposes of this article, we define tear film instability or tear breakup (TBU) to be the state when the tear film becomes sufficiently thin that the tear/air interface reaches the top of the glycocalyx at the ocular surface (King-Smith et al. 2018). However, the common assumption that the lower intensity (seen as the dark area in FL images) implies a thinner tear film is not necessarily true. Choosing an appropriate FL concentration is critical to visualizing the dynamics of the tear film. The FL intensity I depends on both the thickness h' and the FL concentration f' (Webber and Jones 1986; Nichols et al. 2012) as follows:

$$I = I_0 \frac{1 - e^{-\epsilon_f h' f'}}{1 + (f'/f_{cr})^2}. \quad (1)$$

Here, I_0 is the normalization factor, which depends on the optical system, ϵ_f is the Napierian extinction coefficient, and $f_{cr} = 0.2\%$ is the critical concentration. As illustrated in Fig. 1, when we fix I , there exist multiple values of (f', h') that satisfy

Fig. 1 Log–log plot of FL intensity I and dimensionless FL concentration $f = f' / f_{cr}$ with the tear film thickness $h' = 1.5, 3.5, 5 \mu\text{m}$



Eq. (1). With different FL concentrations f' , the corresponding tear film thickness h' varies from less than $1.5 \mu\text{m}$ to more than $5 \mu\text{m}$.

Following Eq. (1), when $f' > f_{cr}$, I decreases quadratically as f' increases; this is the self-quenching regime in Fig. 1. Self-quenching is often used to study the effect of evaporation on the tear film. Previous work has used both low and high FL concentration in healthy subjects to identify the potential mechanism between evaporation and tangential flow for tear thinning in normal eyes (Nichols et al. 2012; King-Smith et al. 2013a). The FL intensity measured from FL images shows a fourfold faster decay rate when using high FL concentration compared with when using low FL concentration. This results supports that evaporation is the main mechanism in those cases. However, if the thinning is caused by tangential flow, f' does not change significantly and the intensity decrease should be similar for both high and low initial conditions.

Different FBUTs for evaporative and rapid thinning may also allow one to identify them in some experiments and subjects. Nichols et al. (2005) measured the thinning rate among different subjects; it is estimated to be between $1 \mu\text{m}/\text{min}$ to $20 \mu\text{m}/\text{min}$. Evaporation thus takes time to thin the tear film. For a tear film with thickness $3.5 \mu\text{m}$, it takes at least 10s for TBU to occur. But in rapid tear thinning, TBU can happen in under a second (King-Smith et al. 2013b; Yokoi and Georgiev 2013b). In evaporative TBU, the tear film thins due to a locally elevated evaporation profile, then the thinning rate slows down due to the growing convergent capillarity contribution; the capillarity contribution is generated by the deformed tear film surface. In rapid thinning, the tear film thins dramatically in the first second, then the thinning rate slows with a weakening divergent tangential contribution from the Marangoni effect and strengthening convergent contribution from capillarity.

From recent subjects, we select one which is thought to have both evaporative tear thinning and tangential-flow-driven tear thinning, but each in different locations. We stabilized the FL images using custom software written in MATLAB (MathWorks, Natick, MA, USA). We monitored the pixel value (FL intensity) at one point by

Fig. 2 Three points selected $i = 1, 2, 3$ for FL intensity extraction are marked by arrows. The initial FL concentration in this subject is estimated to be 0.28%

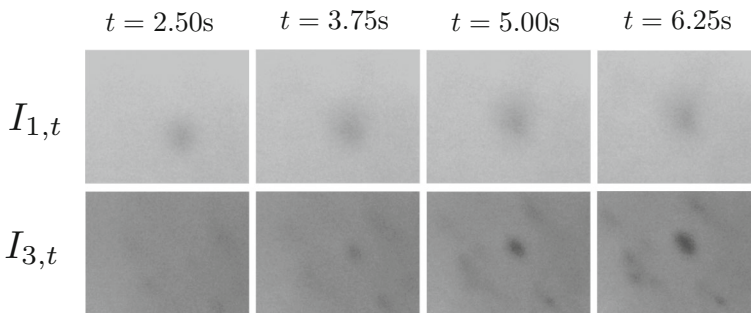
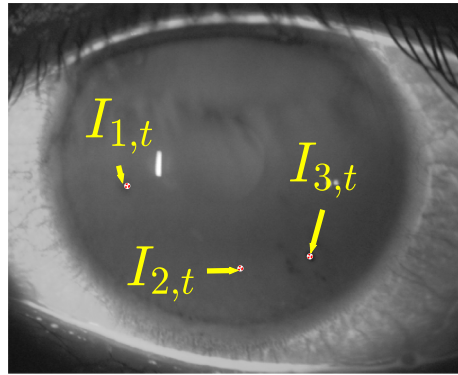
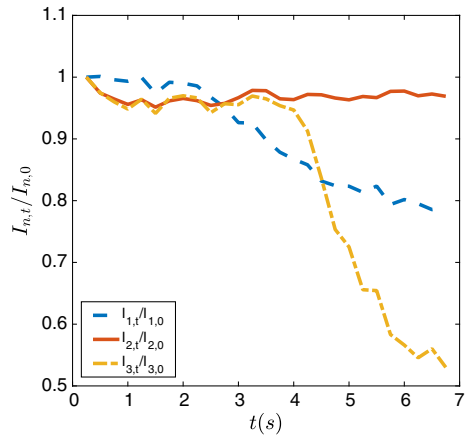


Fig. 3 Sequential images for the suspected evaporative TBU (upper row) and suspected tangential-flow-driven TBU (lower row). Image enhanced for a higher contrast here

averaging the pixel values around it within a radius of 0.037 mm (10 pixels). By averaging the surrounding pixels, we mitigate the noise from both eye movement and fluorescence. Figure 2 shows three locations that were monitored; the circles show the pixels included to approximate the FL intensity at the center. The extracted time series from the imaging data is denoted by $\{I_{i,t}\}$, where $i = 1, 2, 3$ indicates location and t indicates time. Figure 3 shows a sequence of FL images which include the tear thinning for $\{I_{1,t}\}$ and $\{I_{3,t}\}$. It can be seen that a dark spot appears at $t = 2.5$ s in the upper row and at $t = 3.75$ s in the lower row. At $t = 6.25$ s, the dark spot in the lower row grows much darker than in the upper row; the dynamics shown in the lower row is more rapid. We suspect that the upper row is evaporation-driven, while the lower row is tangential-flow-driven. In Fig. 4, we plot the normalized data $\{I_{i,t}\}/I_{i,0}$ with $i = 1, 2, 3$ as in Fig. 2. Location $i = 1$ is suspected to be evaporation-driven; $I_{1,t}/I_{1,0}$ decreases gradually, and the thinning rate decreases with increasing time. Location $i = 2$ serves as background data for comparison, where little thinning occurs. The thinning at location $i = 3$ is suspected to be tangential-flow-driven. One possible cause for the rapid thinning at $i = 3$ is that an air bubble burst in the lipid layer. The air bubble may have stayed in the lipid layer for a time, and then burst, causing a strong outward flow that thins the aqueous layer rapidly (King-Smith et al. 2008, 2013b). Comparing $I_{1,t}$ with $I_{3,t}$, it can be seen that if starting with the same initial

Fig. 4 Time series of FL intensity for three points $i = 1, 2, 3$. $i = 1$ and $i = 3$ are suspected to be evaporative-driven and tangential-flow-driven tear thinning



FL intensity, $I_{1,t}$ will take a much longer time for TBU to occur; $i = 3$ has a much faster relative thinning rate.

Practically, it is difficult to control the initial FL concentration *in vivo* (Mcmonnies 2018). First, the volume of FL solution instilled, or the mass dissolved from an impregnated strip, is uncertain. Second, the tear volume of each subject is unknown; even with the controlled solution volume, the resulting concentration *in vivo* is unknown. However, the initial concentration in mathematical models can be easily set, and it can be shown that different initial concentrations should be considered when imaging TBU caused by different mechanisms. Braun et al. (2014) studied a mathematical model for FL imaging in evaporative TBU with a uniform evaporation rate and a flat tear film. The model conserved water and solutes. For low initial concentration, I remains constant during evaporative thinning. For high initial concentration, I decays with the square of f' due to FL self-quenching. Thus, using FL imaging at initial f' above the f'_{cr} was seen as better for quantifying evaporative tear thinning (Nichols et al. 2012; Braun et al. 2014). Braun et al. (2017) extended the model by including solute transport by advection and diffusion and with a spatially-varying evaporation distribution. Initial FL concentration in the self-quenching regime was best able to match computed tear film thicknesses.

To our knowledge, there is no mathematical model that has investigated FL imaging for rapid tear thinning. Although different hypotheses exist for what causes tangential flow *in vivo*, it has been accepted as a mechanism for rapid tear thinning. There are two main hypotheses for driving forces of tangential flow: (1) dewetting of the corneal surface (Yokoi and Georgiev 2013b) and (2) Marangoni flow induced by non-uniform composition in the lipid layer (King-Smith et al. 2013b, 2018). In this work, we focus on the effect of Marangoni-driven tangential flow on FL imaging for TBU. To simulate a strong tangential flow, we adapted our previous model (Zhong et al. 2018) which captured the rapid thinning caused by a thicker lipid in the lipid layer. With appropriate glob size, the tangential flow generated in our model can thin the aqueous layer to TBU in well under a second, as seen *in vivo*.

3 Model Formulation

To the model of Zhong et al. (2018), we add equations for solute transport in the aqueous layer, specifically for salt ions and fluorescein. We solve the model for the aqueous layer thickness h , pressure p , surface concentration of polar lipid Γ , osmolarity c and FL concentration f . The simulated strong tangential flow allows us to investigate the solutes distribution and resultant FL imaging in rapid tear thinning. The model in this work also adds osmotic flow induced by osmolarity differences between the aqueous layer and corneal epithelium; this flow is estimated to be small in some cases (Nichols et al. 2005) and was neglected in our previous model. However, we can see a contribution in some cases in this paper. In this section, the model is given in axisymmetric cylindrical coordinates in order to simulate the circular-shaped glob. In Cartesian coordinates, the glob is in streak-shaped. More details about derivation of the models are given in Appendices B.5 (spots) and B.2 (streaks).

3.1 Lubrication Theory

The tear film is about $3\text{--}5\ \mu\text{m}$ thick post-blink (King-Smith et al. 2004) yet extends a centimeter over the exposed ocular surface. The thickness (d) compared to its length (ℓ) is thus very small. The value of dimensional parameters can refer to Table 2. The aspect ratio in our scaling is $\epsilon = d/\ell = 0.0471$, which allows us to use lubrication theory to reduce the Navier–Stokes equations and attendant boundary conditions to a manageable problem (Oron et al. 1997; Craster and Matar 2009). The tear film is treated as a single-layer film, and this aqueous layer is considered similar to water with constant density ρ and viscosity μ . The fluid velocity in the spot glob-driven model is denoted $\mathbf{u} = (u_r, u_z)$, which are radial velocity and vertical velocity, respectively. The reduced equations from (2) to (5) enforce conservation of mass for water and solutes in the tear film, as well as the insoluble surfactant on its surface.

$$\partial_t h = -J + P_c(c - 1) - \frac{1}{r} \partial_r (rh\bar{u}), \quad (2)$$

$$\partial_t \Gamma = \left[\text{Pe}_s^{-1} \left(\frac{1}{r} \partial_r (r \partial_r \Gamma) \right) - \frac{1}{r} \partial_r (r \Gamma u_r) \right] B, \quad (3)$$

$$h \partial_t c = \text{Pe}_c^{-1} \frac{1}{r} \partial_r (rh \partial_r c) + Jc - P_c(c - 1)c - h\bar{u} \partial_r c, \quad (4)$$

$$h \partial_t f = \text{Pe}_f^{-1} \frac{1}{r} \partial_r (rh \partial_r f) + Jf - P_c(c - 1)f - h\bar{u} \partial_r f. \quad (5)$$

The dimensionless parameters in these equations are listed in Table 1.

In Eq. (2), J and \bar{u} denote, respectively, the evaporation over the tear film surface and average velocity component along the film in the aqueous layer. Tear thinning is controlled by evaporation, osmotic flow and advection, which are the three terms in the right-hand side of Eq. (2), respectively. $B = B(r)$ in Eq. (3) is a smooth function approximating the step function which is zero on the aqueous/glob region $[0, R_I]$ and unity otherwise:

Table 1 Dimensionless parameters introduced by scaling the model

Parameter	Description	Formula	Value
S	Contribution of surface tension	$\sigma_0 \epsilon^3 / (\mu U)$	1
M	Contribution of Marangoni effect	$\epsilon^2 (\Delta \sigma)_0 / (\mu U)$	1
ϵ	Aspect ratio	d / ℓ	0.0471
A	Non-dimensional Hamaker constant	$A^* / (\epsilon (\Delta \sigma)_0 d \ell)$	2.8571×10^{-4}
P_c	Permeability of cornea	$P_0 V_w c_o / (U \epsilon)$	3.8224×10^{-10}
Pe_s	Contribution of surface diffusion	$\epsilon (\Delta \sigma)_0 \ell / (\mu D_s)$	8.9744
Pe_c	Contribution of salt iron diffusion	$U \ell / D_0$	168.2692
Pe_f	Contribution of FL diffusion	$U \ell / D_f$	690.3353
ϕ	Non-dimensional Napierian extinction coefficient	$\epsilon_f f_{cr} d'$	0.326

The corresponding dimensional parameters can be found in Appendix B.1

$$B(r; R_I, R_W) = \frac{1}{2} + \frac{1}{2} \tanh \left(\frac{r - R_I}{R_W} \right). \tag{6}$$

R_I is the radius for spot glob and R_W is the transition width. During computation, we choose $R_W = 0.05$. B is introduced to smooth the transition between the boundary conditions where the aqueous/air interface and the aqueous/glob interface meet (Zhong et al. 2018). On the aqueous/glob interface, the lipid concentration is high and constant. Outside the aqueous/glob interface (i.e., the aqueous/air interface), the lipid concentration is initially chosen to be lower than within the glob, but it evolves in response to surface transport that is driven by the lipid concentration difference via the Marangoni effect [Eq. (3)]. For salt ions and FL, Eqs. (4) and (5) indicate that evaporation increases the solute concentrations, while osmotic flow decreases solute concentration differences in the aqueous layer. Diffusion smooths out solute variation, while advective flow may increase or decrease concentration at a given location.

The pressure p , average flow \bar{u} and the flow underneath the tear film surface $u_r(r, h, t)$ are given by.

$$0 = p + \frac{1}{r} \partial_r (r \partial_r h) + Ah^{-3}, \tag{7}$$

$$\bar{u} = \frac{-\frac{1}{3} \partial_r p h^2 [B + \frac{1}{4} h(1 - B)] - \frac{1}{2} h B \partial_r \Gamma}{B + (1 - B)h}, \tag{8}$$

$$u_r(r, h, t) = \frac{-\frac{1}{2} \partial_r p h^2 B - \partial_r \Gamma B h}{B + (1 - B)h}. \tag{9}$$

The pressure is generated by the deformed tear film surface as shown in Eq. (7). The average aqueous flow is the sum of two competing contributions, with pressure generated from capillarity and a shear stress generated by the Marangoni effect. The contribution from capillarity grows as tear film deformation grows, and the Marangoni effect weakens when the lipid concentration gradient decreases. These competing

processes lead to the phenomenon that the tear film may thin at small times but then thicken at larger times.

3.2 Evaporation

As in our previous glob-driven model (Zhong et al. 2018), we consider four different evaporation distributions based on different hypotheses on the composition of the glob. However, we want to compare our results to results from an evaporation-driven spot model with elevated water loss in a central region (Braun et al. 2017). Thus, we choose a similar evaporation flux where the evaporation rate is high over the aqueous/glob interface and low over the aqueous/air interface, namely

$$J = (1 - B)v_{\max} + Bv_{\min}. \quad (10)$$

Here, $v_{\max} = 10 \mu\text{m}/\text{min}$ and $v_{\min} = 1 \mu\text{m}/\text{min}$. We discuss the numerical results with other types of evaporation distribution from (80) to (83) in Sect. 4.9.

3.3 FL Intensity

The FL intensity I can be evaluated via the following non-dimensional version:

$$I = I_0 \frac{1 - e^{-\phi fh}}{1 + f^2}. \quad (11)$$

Here, ϕ is the non-dimensional Napierian extinction coefficient.

We aim to show that Eq. (11) has important consequences for understanding FL imaging of TBU. For many cases of TBU, evaporation is the primary mechanism (Braun et al. 2015; King-Smith et al. 2018). When evaporation thins the tear film, it also increases the FL concentration. If the initial FL concentration is at the critical concentration f_{cr} or larger, FL self-quenching occurs and I decreases quadratically as f increases. In that regime, \sqrt{I} can approximate the tear film thickness h well. However, in rapid thinning caused by tangential flow, the tangential flow redistributes water in the aqueous layer without changing the concentration. If evaporation is not taken into consideration, FL concentration stays constant. For a fixed FL concentration f , expanding for small h yields a leading term proportional to f and h (Braun et al. 2014). Therefore, we expect I to be proportional to h in our model when evaporation is unimportant, in contrast to the evaporative case. In vivo, both situations and the possible combination of the two may need to be considered.

3.4 Initial and Boundary Conditions

The boundary and initial conditions are quite similar to those in Zhong et al. (2018). At the center of glob $r = 0$, the boundary conditions enforce symmetry and thus no flux via

$$\partial_r h = \partial_r p = \partial_r \Gamma = \partial_r c = \partial_r f = 0. \quad (12)$$

We assume the domain is sufficiently long and there is no flux at $r = R_L$. We end up with the same boundary condition as Eq. (12) there.

For the initial conditions, all dependent variables except for the surfactant concentration are assumed to be spatially uniform; with our scalings, these become, on $0 \leq r \leq R_L$,

$$h(f, 0) = c(r, 0) = f(r, 0) = 1, \quad \text{and} \quad p(r, 0) = -A. \quad (13)$$

The pressure is consistent with the initial thickness via Eq. (7). We assume that the glob has high surfactant concentration and the mobile tear/air interface outside of it has a lower concentration initially. From our scalings, $\Gamma = 1$ under the glob and $\Gamma = 0.1$ outside the glob. Using the transition function $B(r)$, the initial condition for Γ is then

$$\Gamma(r, 0) = 1 \cdot [1 - B(r)] + 0.1 \cdot B(r). \quad (14)$$

3.5 Numerical Methods and TBU Definition

We solve the model numerically as follows. The spatial derivatives in the PDE system given by Eqs. (2)–(9) are first discretized using Chebyshev spectral method (Trefethen 2000) and collocated on second kind points. The resulting equations are a system of resulting differential algebraic equations (DAEs) the dependent variables at the grid points r_i or x_i , $i = 1, \dots, n$ are then $h_i(t)$, $\Gamma_i(t)$, $c_i(t)$, $f_i(t)$ and $p_i(t)$; the first four have time derivatives, while the last does not. The boundary conditions become algebraic conditions that are applied at the ends instead of applying the DAEs there. The initial conditions are applied at $t = 0$. The DAE system is solved in MATLAB using `ode15s`. We choose a long enough domain such that the results are insensitive to it. Equation (11) is used after the solutions for $h_i(t)$ and $f_i(t)$ are found.

The simulations are run until TBU occurs in the model. We define TBU to be when tear film surface, which may be either the aqueous/glob interface or the aqueous/air interface, reaches the estimated thickness of glycocalyx (King-Smith et al. 2018); we assume a representative value of $0.25 \mu\text{m}$ (Gipson 2004) for this thickness. Thus, when the minimum tear film thickness $\min_i h_i(t)$ decreases to $0.25 \mu\text{m}$ (or 0.071 non-dimensionally), the simulation stops.

4 Results

The results of the spot model are discussed in Sects. 4.1–4.9. In Sect. 4.10, we show similar results from the streak model. In all the figures presented in this section, the time shown in the y-axis label has units of seconds.

4.1 TBU Dynamics and Solutes

In Fig. 5, we show computed results for the aqueous layer thickness h , surfactant (polar lipid) concentration Γ , osmolarity c , fluorescein concentration f and scaled FL

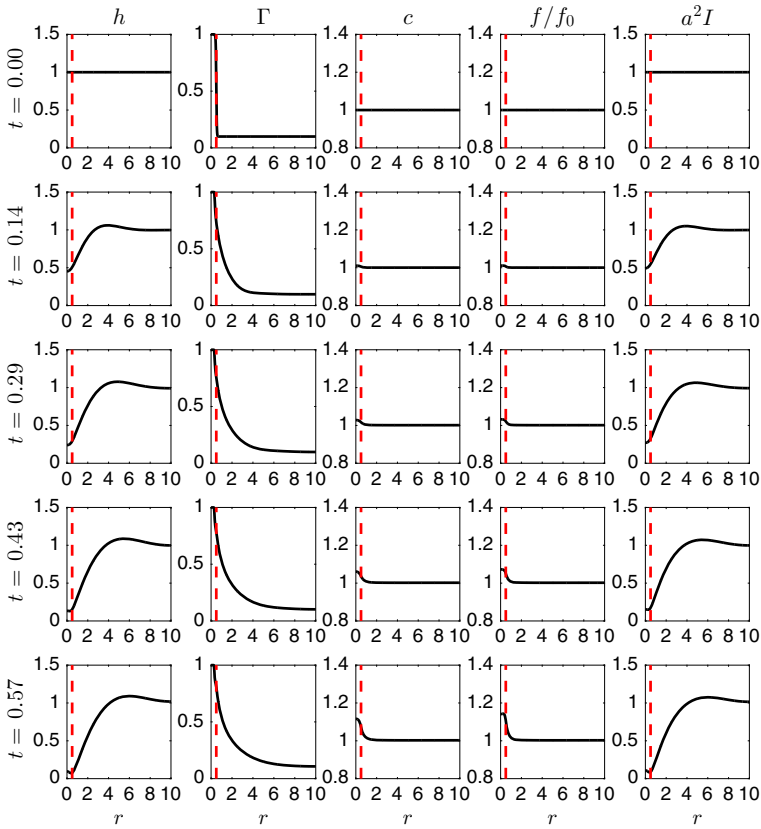


Fig. 5 Dynamics of tear thinning and solute transport with $f_0 = 1$, $R_I = 0.5$ and evaporation as in Eq. (10). From left to right, the columns plotted are thickness, surfactant concentration, osmolarity, scaled FL concentration and scaled FL intensity. Each row is at a different time (in seconds). The vertical dashed line represents the glob edge at R_I

intensity $a^2 I$, in columns from left to right. Different times are shown in each row. Here, $a = 1/\sqrt{I(r, 0)}$ is a constant that we choose to match the intensity with the initial aqueous layer thickness with initial FL intensity. In this case, the dynamics of TBU are very similar to previous results when osmolarity and fluorescein are neglected (Zhong et al. 2018); the tear film thins rapidly at the center of the glob, and at $t = 0.57$ s, TBU occurs. The rapid thinning is caused by the strong tangential flow driven by the appreciable gradient in Γ as shown in the second column; the flow and concentration gradient are linked via the Marangoni effect. The third and fourth columns in Fig. 5 indicate that the concentrations of solutes (f and c) only increase slightly. The osmotic flow induced by the (slightly) higher osmolarity (third column) in the aqueous layer is too weak to slow down the rapid thinning. The TBUT is the same whether we include and exclude the osmotic flow here. The solute concentrations in the aqueous layer change slightly due to (1) tangential flow that carries solutes when redistributing the aqueous layer, and (2) evaporation which thins the tear film via water loss and increases

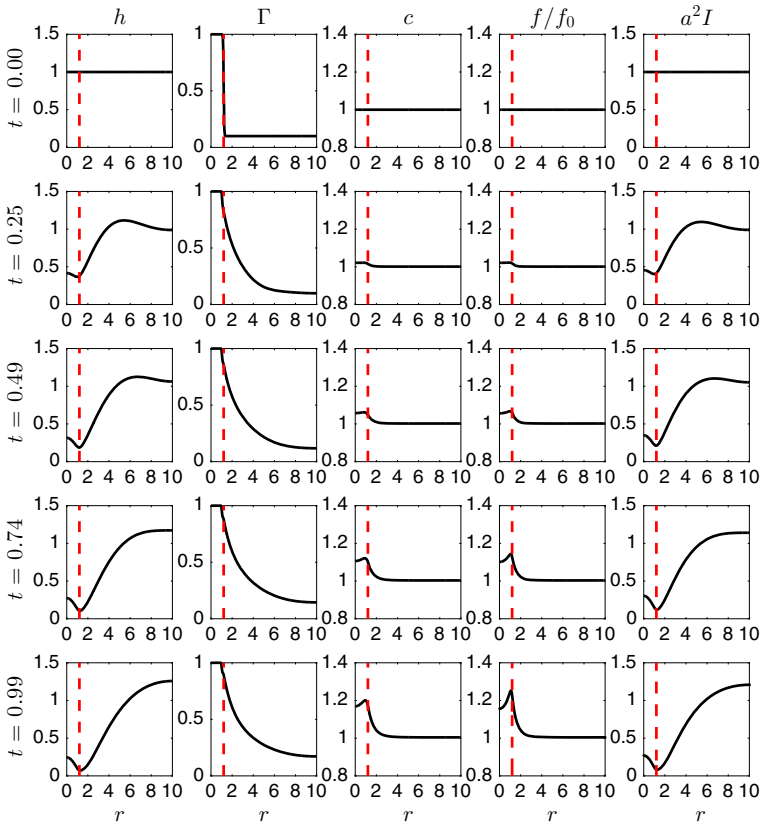


Fig. 6 Dynamics of tear thinning and solutes transport, when $f_0 = 1$ and $R_I = 1.2$. The columns are rows as in Fig. 5

the concentration of solutes. However, TBUT for rapid breakup is usually in under a second, which only allows evaporation to slightly increase the solute concentrations. In the last column, the scaled FL intensity I has the roughly the same shape as the aqueous thickness h , which shows that FL intensity approximates the tear film thickness well.

In Fig. 6, we plot dynamics of TBU when the glob size is increased to $R_I = 1.2$. Within a range, TBUT increases as R_I increases (Zhong et al. 2018); here TBUT increases to 0.99s because R_I is in that range. When compared with $R_I = 0.5$, the longer TBUT allows time for evaporation to change the c and f . We find that the salt ions have a lower concentration than fluorescein due to a roughly four times larger diffusion coefficient (and similarly smaller Peclet number). The peak value of c and f are located as a result of the thinner tear film there: the elevated evaporation rate over the glob loses the same amount of water into the ambient air, but relative changes in thickness are large where the aqueous layer is thin. Thus, both c and f are elevated but f increases more in the thinner tear film because it diffuses slower than c . This is consistent with previous results (Peng et al. 2014; Braun et al. 2017).

4.2 Diffusion Versus Advection

For rapid tear thinning, fast tangential flow is the primary mechanism; evaporation plays a role but has an unimportant contribution in this case. The different primary mechanisms for evaporative TBU and tangential flow leads to different conclusions regarding fluorescent imaging. To better understand the contributions to transport of solutes in the aqueous layer, we plot the average aqueous velocity, the diffusion term and the advective terms in Eqs. (4) and (5) for the results of Fig. 6. The diffusion terms for the osmolarity and fluorescein are

$$-\frac{1}{\text{Pe}_{cr}} \partial_r (rh \partial_r c) \quad \text{and} \quad -\frac{1}{\text{Pe}_{fr}} \partial_r (rh \partial_r f). \quad (15)$$

The advective terms are

$$\bar{u}h \partial_r c \quad \text{and} \quad \bar{u}h \partial_r f. \quad (16)$$

Figure 7 shows h and $10\bar{u}$ in the first column. The positive average aqueous velocity for all times indicates that the Marangoni effect always dominates the thinning process. At the beginning, the Marangoni effect is so strong that a tall spike in the \bar{u} formed at the glob edge. As the lipid spreads out, the lipid concentration difference decreases and the outward velocity weakens around the glob edge. At the same time, the capillary flow grows stronger due to a more deformed tear film surface. The flow, however, stays positive and decreases as time goes on. The second and third columns plot the diffusion and advection terms for c and f . It is shown that the advection term is larger than the diffusion term at the beginning. As \bar{u} weakens and local c and f values increase from evaporation, the diffusion term becomes comparable to and grows larger than advection at $t = 0.49$ s for c and $t = 0.99$ s for f . The smaller diffusion coefficient for fluorescein is responsible for the time delay.

The sign of the advection flow switches across the glob edge in the last two rows in Fig. 7 (see right column). Based on the first column, the average aqueous flow pushes the water from left to right. The peak concentration for solutes formed at the glob edge at $t = 0.5$ s as shown in Fig. 6. To the left of the peak, the outward flow mixed the tears of lower concentration with the tears of higher concentration, which decreases the concentration on the left region. To the right of the peak, a similar but a converse situation occurred.

4.3 Distribution of Solutes

Figure 8 shows the distribution of salt and fluorescein ions with small ($R_I = 0.5$) and large ($R_I = 3.2$) glob sizes. The quantities ch and fh are plotted, which can be thought of as the mass of solutes at each location (Braun et al. 2015, 2017). In both plots, the mass distribution roughly matches the shape of the tear film and the minimum mass of solutes occurs near the glob edge. The dominant mechanism of tangential flow determines the shape of the tear film and has a significant influence on the solute distributions. Three effects contribute. (1) The tangential flow thins the aqueous layer rapidly around the glob edge. Because it is a fast process, the distributions for solute

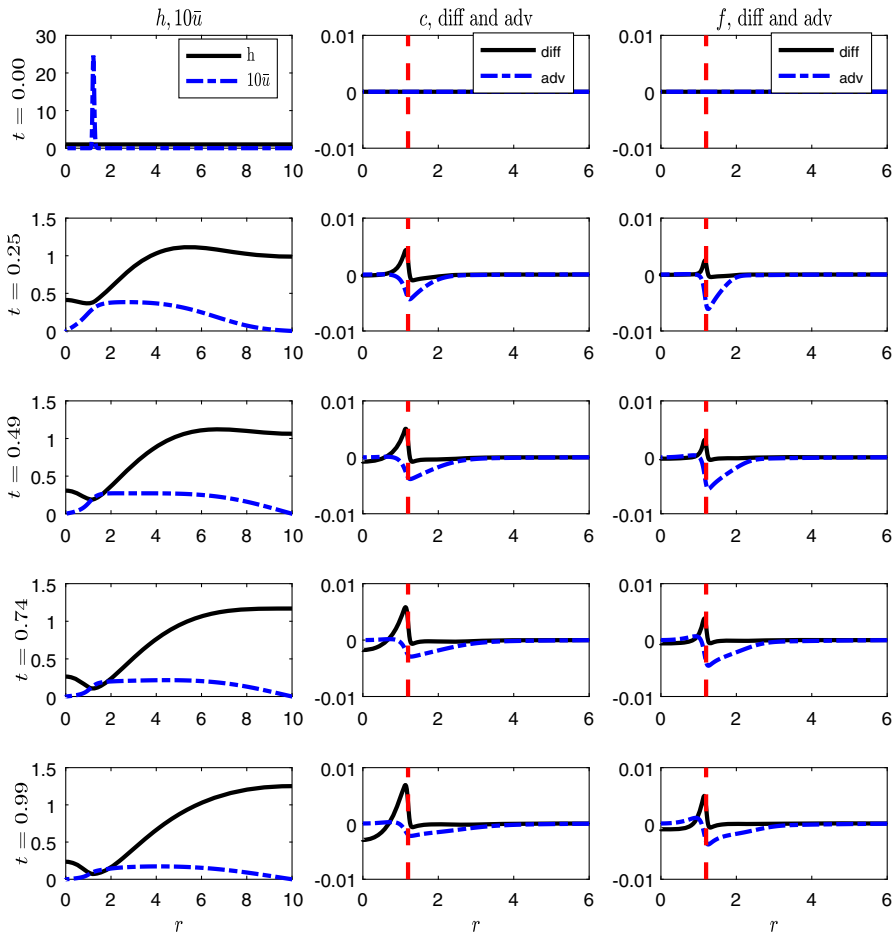


Fig. 7 Thickness, \bar{u} , diffusion terms [Eq. (15)] and advection terms [Eq. (16)] for rapid tear thinning for $R_I = 1.2$, $f_0 = 1$ (Fig. 6)

mass mimic the tear film. (2) Evaporation increases the concentration of solutes, which may increase the solutes concentration at the thinnest film locations due to the large relative loss of water there. However, in this case, there is little effect. (3) The non-uniform distribution of the solute concentrations may induce diffusion and reduce the mass of solutes around peak concentration values which may be under the glob or near its edge. TBUT for $R_I = 0.5$ is 0.57s and the TBUT for $R_I = 3.2$ is 4.97s; since evaporation and diffusion happen slowly compared to the thinning from tangential flow, the effect of diffusion in the upper row ($R_I = 0.5$) is difficult to see. If we compare the plots in the bottom row ($R_I = 3.2$), we observe a higher local maximum for ch at $r = 0$ and a smaller local minimum near the glob edge. Those differences are the result of faster diffusion. A more pronounced example of the effect of diffusion will be shown in Fig. 19 from the streak model.

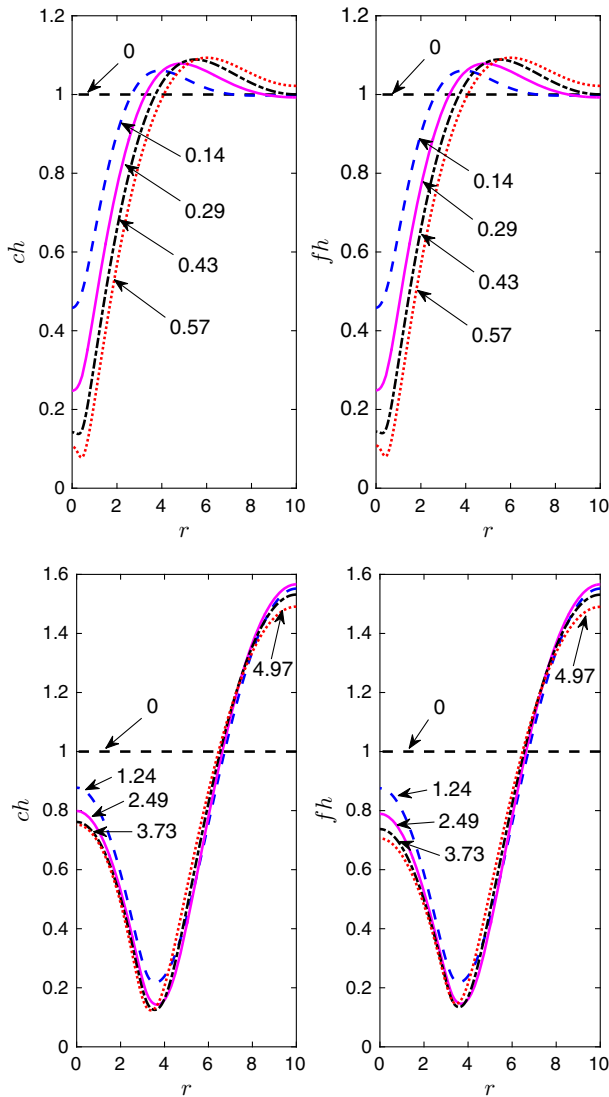


Fig. 8 The solute mass distribution of solute mass for spot size $R_I = 0.5$ (upper row) and $R_I = 3.2$ (lower row). In all plots, the initial FL concentration $f_0 = 1$. The time in seconds for each curve is marked as a number with arrow

4.4 Extrema as a Function of Time

Figure 9 shows the value of the minimum aqueous layer thickness, maximum fluorescein concentration and osmolarity as functions of time with different glob sizes $R_I = 0.5$, $R_I = 1.5$ and $R_I = 2.5$. The extrema functions are defined as follows:

$$h_{\min}(t) = \min_{r \in [0, R_L]} h(r, t), \quad c_{\max}(t) = \max_{r \in [0, R_L]} c(r, t) \quad (17)$$

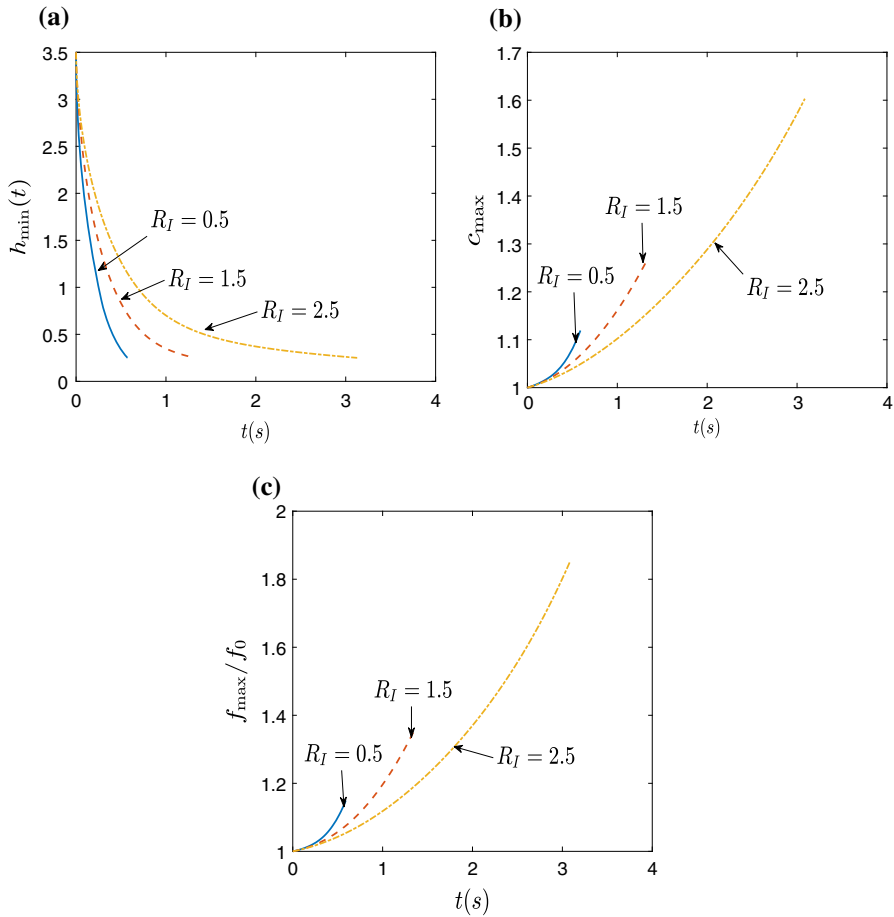


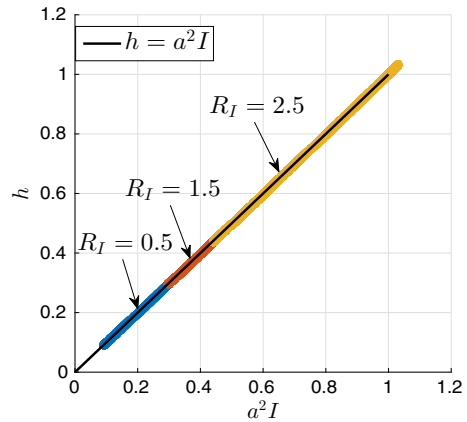
Fig. 9 Extrema of h (upper left), c (upper right) and f (lower right) as functions of time with $f_0 = 1$ for glob sizes $R_I = 0.5, 1.5, 2.5$

and

$$f_{\max}/f_0(t) = \max_{r \in [0, R_L]} f(r, t)/f_0. \tag{18}$$

The minimum thickness plot is at the upper left. Initially, the tangential flow for different glob sizes is very strong, which thins the aqueous layer rapidly at a similar rate. However, for smaller globs, there is less water under the glob, which leads to a faster thinning rate and shorter TBUT compared to larger globs. As illustrated in Fig. 9, for a fixed glob size, the maximum osmolarity (upper right) and fluorescein concentration (lower right) increase at a faster rate as time increases. The increasing growth rate here is the result of thinner aqueous layer at a later time; the assumed fixed rate of evaporation increases solute concentration more where the tear film is thinner. This also explains why the smaller glob corresponds to a faster increase of solute concentrations. The thinner aqueous layer also has a slower transport of solute

Fig. 10 Scatter plot of the tear film thickness and scaled FL intensity when glob has size of $R_I = 0.5, 1.5, 2.5$ with $f_0 = 0.1$



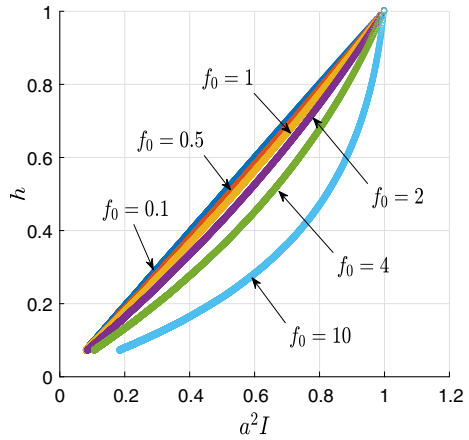
which helps keep solutes localized there. Since salt ions diffuse faster than FL, the maximum c is lower than the maximum f .

4.5 Relationship Between FL Intensity and Aqueous Thickness

The FL intensity I is measured by clinicians and is interpreted as tear film thinning. For our purposes, it is the pixel value of grayscale versions of the FL images from the clinic. In our model, given Eq. (11), we can evaluate the FL intensity with the computed f and h . To observe how I approximates h , we created a scatter plot of the aqueous layer thickness at the glob center $h(0, t)$ and its scaled FL intensity $a^2 I(0, t)$ in Fig. 10. We choose a dilute initial FL concentration, $f_0 = 0.1$ (0.02% in dimensional terms) computed results for three values of R_I . Figure 10 shows that FL intensity is roughly a linear approximation to the aqueous layer thickness, when glob size is in the range $0.5 \leq R_I \leq 2.5$. The TBUT increases from 0.57 to 3.13 s, but these relatively small values do not allow f to change much. With a roughly fixed and small f , the exponential term from Eq. (11) can be expanded for small exponent h , which yields the linear relationship between I and h . For $R_I = 0.5$, the aqueous thickness decreases rapidly and monotonically to TBU at the glob center, and both c and f remain quite close to unity. For $R_I = 2.5$, the central aqueous thickness can first increase above unity (Fig. 10), which indicates the aqueous layer at the glob center first thins by the divergent Marangoni-driven tangential flow and is then increased modestly by some evaporation and capillary-driven tangential flow (capillary flow; Zhong et al. 2018,).

In Fig. 11, we fixed $R_I = 0.5$ and varied the initial FL concentration from very dilute $f_0 = 0.1$ to high $f_0 = 10$, which are 0.02% and 2% in dimensional terms. As illustrated in Fig. 11, when the initial FL concentration is smaller than the critical concentration $f_{cr} = 0.2\%$, FL intensity can roughly linearly approximate aqueous layer thickness. Otherwise, the relationship is not linear and it becomes more difficult to relate I and h . When f is large, the linear relationship fails.

Fig. 11 Scatter plot of the tear film thickness and the scaled FL intensity when glob size is $r_I = 0.5$ with initial FL intensity $f_0 = 0.1, 0.5, 1, 2, 4, 10$



4.6 Intensity and Thickness Distribution

Braun et al. (2014, 2017) point out that \sqrt{I} approximates h better when using initial FL concentrations at about the critical concentration (0.2%) or higher for evaporative TBUs; f increases due to evaporation, and this causes self-quenching (Webber and Jones 1986; Nichols et al. 2012). In the self-quenching regime, I decreases quadratically in f as the tear film thins. For a spatially uniform film and evaporation, $f(t)h(t) = f_0$ at all times with our scalings, and approximating Eq. (11) yields $h \propto \sqrt{I}$. However, in rapid tear thinning, the solute concentrations only vary slightly and we expect $I \propto h$ with dilute FL as in Fig. 5. In Fig. 12, we compare h , I and \sqrt{I} at the TBUT to evaluate these approximations. The upper row corresponds to a smaller glob size $R_I = 0.5$ with TBUT = 0.57 s; the lower row corresponds to $R_I = 2.5$ with TBUT = 3.13s. Comparing the upper row with the lower row, we can see some influences from evaporation on the bottom row. Comparing the left column with the right column, we study the difference between using FL with low concentration ($f_0 = 0.1$ or 0.02%) and high concentration ($f_0 = 2$, or 0.4%).

In all cases in Fig. 12, $a^2 I$ estimates h better than $a\sqrt{I}$, which implies that tangential flow drives TBUs and FL quenching does not occur. The approximations in the upper row outperforms those in the lower row. When TBUT = 0.57 s, I approximates h well even when $f_0 = 2$ as illustrated in the upper right plot. The longer TBUT = 3.13 s allows water to escape via evaporation and the solute concentrations increase somewhat. In the lower left plot, $a^2 I$ approximates h well except in the TBUT region, where f increases more obviously; the concentrated FL under the aqueous/glob interface corresponds to a smaller absorbance (which increases $1 - \exp^{-\phi f h}$), resulting in a higher intensity there.

Comparing the left column with the right column, the FL intensity approximates the thickness better with dilute FL concentration. When the initial FL concentration is small, the FL concentration increases less under the same evaporation. For example, if we only consider evaporation, when the tear film thins to half of its thickness, the FL concentration is doubled. If $f_0 = 0.1$ the doubled FL concentration is $f = 0.2$. If $f = 2$, the doubled FL concentration is $f = 4$. Following the same reasoning, for

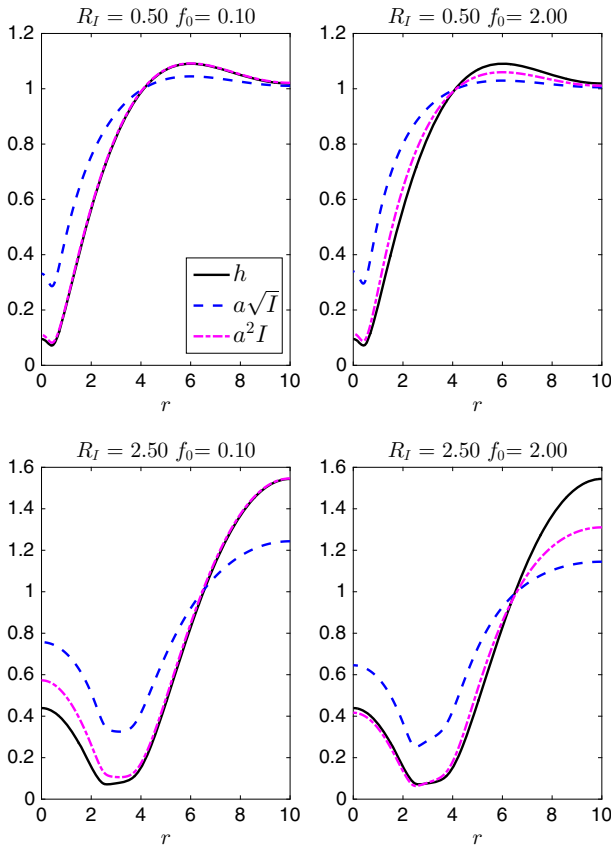


Fig. 12 Aqueous layer thickness and its approximation with $a\sqrt{I}$ and a^2I for initial FL concentration $f_0 = 0.1$ (left column) and $f_0 = 2$ (right column). Top row, $R_I = 0.5$; bottom row, $R_I = 2.5$

a dilute FL, if TBUT is short, f can be roughly considered as a constant. The tear film thickness can then be well approximated by I , which is shown in the upper left plot in Fig. 12. In the upper right plot, when a higher f_0 is utilized, the linear relation between I and f breaks slightly. Comparing the lower left with the lower right plot, we observe a downward shift in the right plot. The shift makes the estimation fit the TBU region better. When a concentrated FL is utilized, the estimation becomes smaller due to a larger FL efficiency ($1/(1 + f^2)$). In some cases in clinics, ophthalmologists are more interested in estimation of tear film thickness for the TBU region rather than the overall estimation. In this case, a concentrated FL will be a better choice.

4.7 Error of Approximation with Initial FL Concentration and Glob Size

We define the ℓ_2 norm

$$E_2 = \|\mathbf{h}(\mathbf{r}, \text{TBUT}) - a^2\mathbf{I}(\mathbf{r}, \text{TBUT})\|_2 \quad (19)$$

Fig. 13 Approximation error as a function of initial FL concentration for $R_I = 0.6$ (TBUT = 0.60 s)

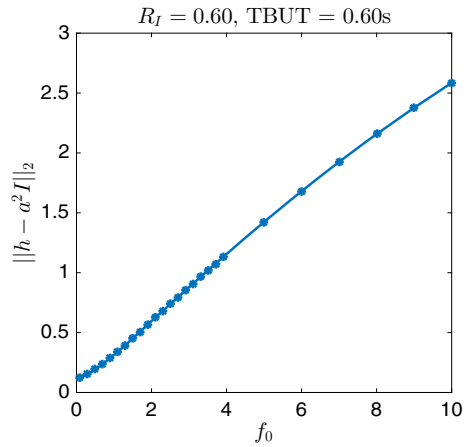
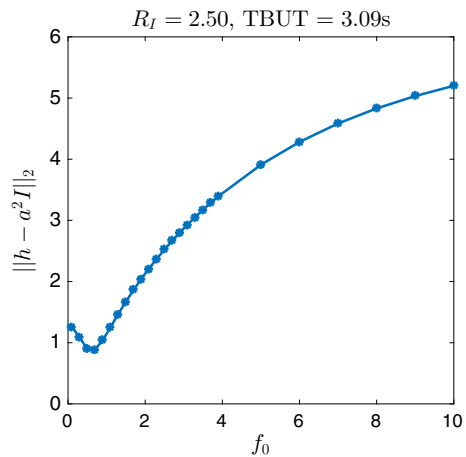


Fig. 14 Approximation error as a function of initial FL concentration for $R_I = 2.5$ (TBUT = 3.09 s)



to be the measure of the error at TBUT. Here, $\mathbf{r} = \{r_j\}$ is the vector of grid points; $\mathbf{h} = \{h(r_j, \text{TBUT})\}$ and $\mathbf{I} = \{I(r_j, \text{TBUT})\}$ are the vectors of each variable at the grid points. Figures 13 and 14 show the relationship between initial FL concentration and corresponding error for TBUT = 0.6 s and TBUT = 3.09 s. When TBUT is short, the most dilute FL gives the best approximation; the small FL concentration is roughly constant across the domain $[0, R_L]$, and evaporation is negligible. Increasing f_0 magnifies the changes across the domain and also corresponds to a larger error in linearizing the absorbance term. In Fig. 14, TBUT is larger and the error decreases for smaller f_0 , then increases with increasing f_0 . This increase is caused by concentration increases due to evaporation.

4.8 Time Sequence

In clinics, ophthalmologists track the formation of TBU until the moment when they observe the first dark spot. Practically, it is difficult to quantitatively determine FBUT

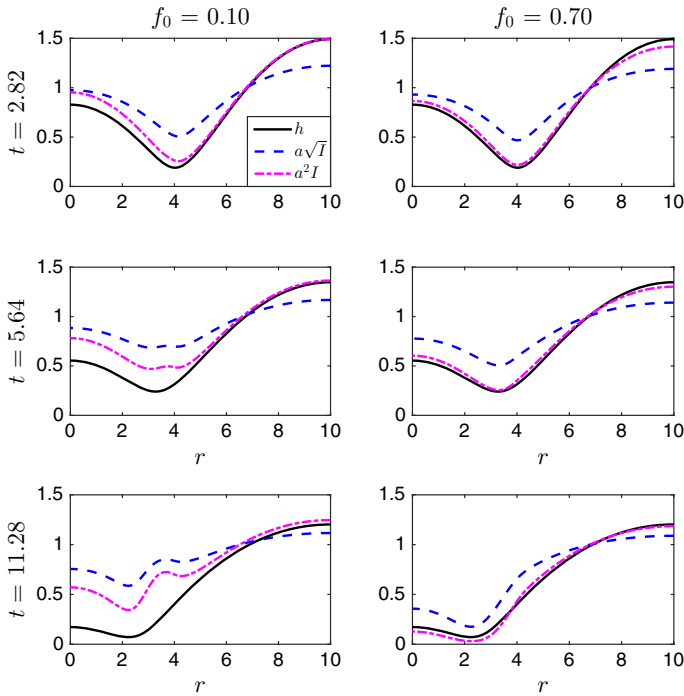


Fig. 15 Time sequence of tear thinning and its approximation using FL intensity, when $R_I = 4$ and TBUT = 11.28 s. The two initial FL concentrations shown are $f_0 = 0.1$ and $f_0 = 0.7$. Each row is at a different time in seconds

because the FL intensity may not accurately represent the tear film thickness (Braun et al. 2015; King-Smith et al. 2018). In Fig. 15, we plot the time sequence of the approximation to the tear film thickness using FL intensity to simulate the observation process. In order to have significant tangential flow, evaporation and diffusion together, we choose a large glob, $R_I = 4$; the long TBUT (11.28 s) takes enough time for evaporation and diffusion to contribute to the dynamics. The two columns in Fig. 15 have the same (fluid) dynamics for tear thinning but different initial FL concentrations f_0 are used. In both columns, divergent tangential flow (driven by Marangoni effect) thins the aqueous layer rapidly in the first row. Then, the Marangoni effect dies away and the convergent tangential flow (due to the capillary effect) overcomes it. Fluid is pushed into the thinnest area which may increase the amount of fluid. If we compare the aqueous layer thickness in the first row at $t = 2.82$ s with the second row at $t = 5.64$ s, the thinnest location shifts to the left and the aqueous layer at the previously-thinnest location thickens slightly. TBU occurs at $t = 11.28$ s due to evaporation. In the first row, the main mechanism is tangential flow and in the last row the dominant mechanism is evaporation. We can consider TBU in the last row to be caused by a mixed mechanism combining the Marangoni-driven tangential flow and evaporation.

In the left column, a dilute f_0 is used, and the approximation of the aqueous layer thickness is larger than the computed tear film thickness. In this case, the theory predicts that observed FBUT *in vivo* would be longer than the real TBUT because the

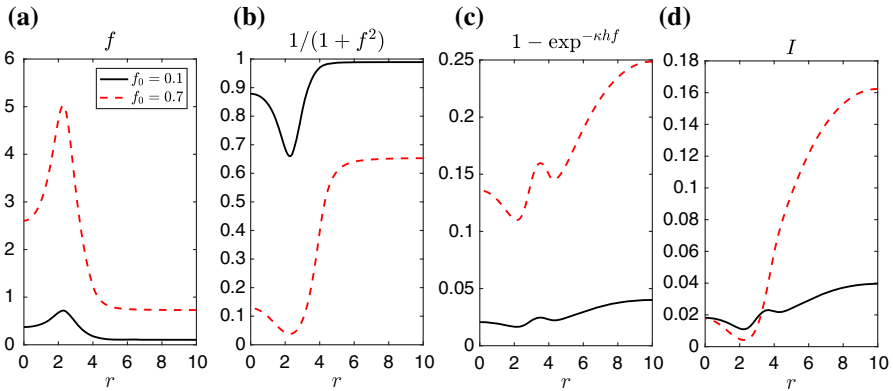


Fig. 16 From left to right, we plot the FL concentration and various parts of Eq. (11). **a** f ; **b** efficiency; **c** absorbance; **d** I at $t = \text{TBUT}$

higher FL intensity suggests a thicker aqueous layer. In the second row of the first column, there is a localized bump in I and \sqrt{I} above the thinning region. The bump corresponds to a local increase in f as illustrated in the leftmost figure in Fig. 16. The local increase is caused by advection and diffusion. As in Figs. 5 and 7, advection brings solutes toward the glob edge, and evaporation removes water, which elevates solute concentration. Diffusion away from the region is too slow to smooth out the bump in this case.

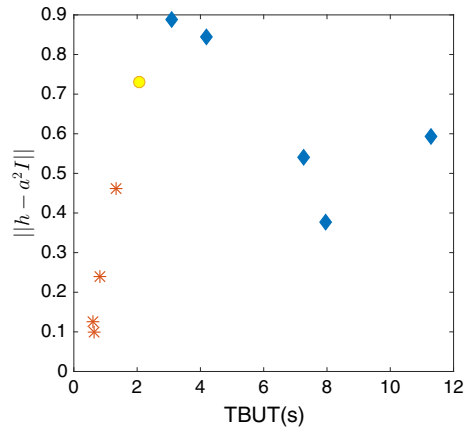
In the right column, a higher f_0 is used. As shown in Fig. 16c, the distribution of solute mass for $f_0 = 0.7$ has a more obvious hill. However, the higher concentration caused a much smaller efficiency which effectively canceled out the hills in I . As a result, $f_0 = 0.7$ approximates the aqueous layer thickness very well. Another reason for this better approximation is that f is close to or above the critical concentration in the TBU region.

Figure 15 shows the deviation introduced by evaporation. The approximation of the aqueous layer thickness gets worse as time increases in both columns. In rapid tear thinning, the FL intensity decreases rapidly and dark areas formed quickly in the FL images. In experiments, TBU in Fig. 15 may reasonably be concluded with FBUT = 2.82 s; the tear film is already very thin and the TBU region would appear dark. However, the model shows h is still well above our threshold for TBU. Evaporation takes an extra 8.46 s to overcome the capillary flow and reduce the tear film to the 0.25 μm threshold. From these results, we conclude that a dilute concentration such as $f_0 = 0.1$ can still be considered a good choice for measuring very rapid TBU. However, if the TBUT is larger and the suspected mechanism is primarily tangential flow, then a concentration near but slightly lower than f_{cr} may be better to both avoid the small hills and to obtain a generally brighter image.

4.9 Evaporation

When TBUT is long, the most dilute FL is no longer the best choice. The TBUT varies from 0.6 to 11.28 s for R_I in the range 0.2 to 4 (Zhong et al. 2018); the longer TBUTs

Fig. 17 Lowest error of approximation E_2 as a function of TBUT for spots; each symbol comes from minimizing over f_0 at a given R_I . The symbols give the best f_0 : *, $f_0 = 0.1$; \circ , $f_0 = 0.5$; \diamond , $f_0 = 0.7$



allow for evaporation to make a non-negligible contribution. We quantify how well $a^2 I$ approximates the computed thickness h for different glob sizes and initial FL concentrations by finding the minimum error for a fixed glob size; varying the glob size. To find the minimum approximation error at each fixed glob size, we vary f_0 from 0.01 to 10 in steps of 0.1, and note value of f_0 with the lowest value of E_2 . To relate the results more closely to in vivo results, Fig. 17 shows the lowest error at each TBUT. The different symbols indicate the f_0 that yielded the minimum error. It can be seen that when TBUT is less than 2 s, a dilute concentration $f_0 = 0.3$ is the best choice. When TBUT is longer than 4 s, $f_0 = 0.7$ is the best choice for visualizing TBU. Figure 15 is one example where $f_0 = 0.7$ performs better than $f_0 = 0.3$.

We also tried different evaporation distributions than the default case. Three different distributions, given by Eqs. (80)–(83), were also studied. As found in Zhong et al. (2018), different evaporation distributions will not dramatically change the dynamics when tangential flow dominates the thinning process. However, evaporation is the force that drives increases of solute concentration, and the increase is faster where the tear film is thinner because the relative change in thickness is largest at the thinnest locations. As shown in Fig. 18, f increases where there is nonzero evaporation and the peak value occurs around the glob edge where the tear film is thinnest. Although the solute concentration distribution differs mildly for different evaporation distributions, the approximations to h using I are similar, since the dynamics of the tear thinning are similar.

4.10 Comparison Between Streak and Spot Models

When comparing mass distribution in the spot and the streak model with similar TBUT in Figs. 8 and 19, we found streak model corresponds to a stronger diffusion. The difference between the distribution of ch and fh in Fig. 19 at TBUT = 4.65 s is easier to tell than in Fig. 8 at TBUT = 4.97 s.

In order to find the best value of f_0 to use when visualizing streaks, we used the same process as in Fig. 17. We varied X_I from 0.1 to 2 in steps of 0.1, and at each

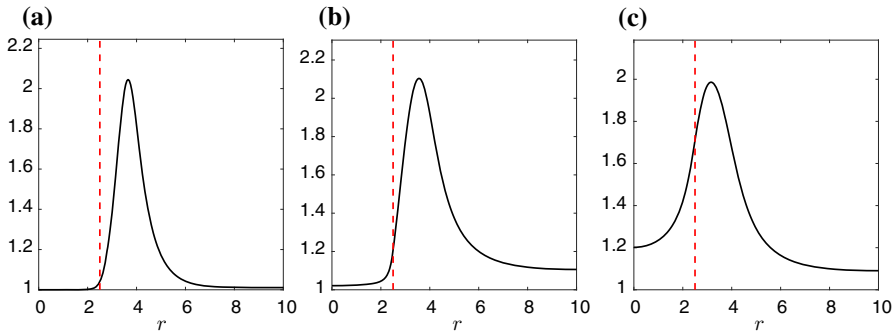
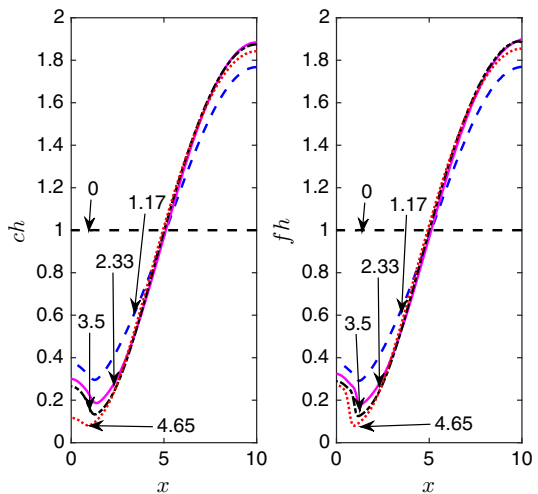


Fig. 18 f/f_0 at $t = \text{TBUT}$, when $R_I = 2.5$ with different evaporation distributions: **a** Eq. (80); **b** Eq. (82); **c** Eq. (83)

Fig. 19 Distribution of masses ch and fh when the streak half width is $x_I = 1.1$ with $f_0 = 1$. The time in seconds for each curve is marked with a number with arrow

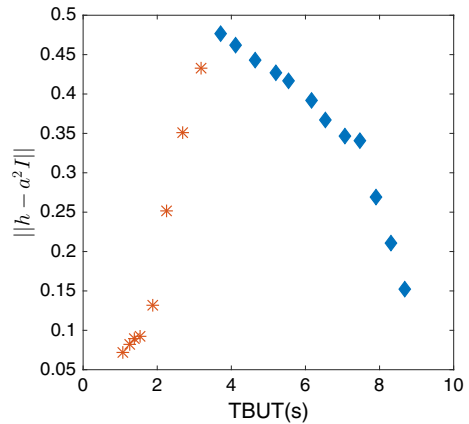


X_I we varied f_0 to find the lowest value of E_2 (Eq. 19). Figure 20 shows the results. For shorter TBU, a dilute $f_0 = 0.1$ returns the best approximation. When TBUT is greater than 4 s, a slightly higher concentration of $f_0 = 0.5$ appears to best according to the theory.

5 Discussion

We studied the dynamics of solutes in the aqueous layer with a strong tangential flow driven by the Marangoni effect from non-uniform lipid distribution. We adapted our previous model which tries to capture the tangential flow induced by a glob in the lipid layer (Zhong et al. 2018). The model hypothesis is based on an experimental phenomenon where the rapid thinning region correlates with a thicker lipid layer. The phenomenon is observed in simultaneous images of fluorescence and the tear film lipid layer (TFLL) (King-Smith et al. 2013b); the FL images shows the thinning of

Fig. 20 Lowest error of approximation E_2 as a function of TBUT for streaks; each symbol comes from minimizing over f_0 at a given X_I . The symbols give the best f_0 : *, $f_0 = 0.1$; \diamond , $f_0 = 0.5$



the tear film and the images of TFLI show the simultaneous lipid layer thickness. The lipid layer was simplified to an insoluble surfactant on a deforming free surface with tangentially immobile and mobile regions.

The strong tangential flow causes rapid tear thinning; with appropriate glob size, TBU occurs in under a second as seen *in vivo*. The strong tangential flow drives aqueous fluid from under the glob to surrounding region without changing the concentration of solutes in the aqueous layer. As shown in Fig. 8, the solutes' mass distribution is proportional to the shape of the tear film; the effects of evaporation, capillarity and diffusion are relatively unimportant in this case due to the short time for rapid tear thinning. As a result, the FL intensity is roughly proportional to the aqueous layer thickness when a dilute initial FL concentration f_0 is used. This linearity allows us to approximate the tear film thickness h using the FL intensity I . We tried different evaporation distributions; the approximations to the tear film thickness using FL intensity vary slightly but are very similar.

During strong tangential flow, the solute transport is dominated by advection and the solute concentrations are effectively constant. If the initial FL concentration is lower than the critical concentration $f_{cr} = 0.2\%$, this leads to a linear relationship between I and h as shown in Fig. 10. The shorter timescale of tangential-flow-driven tear thinning corresponds to fast thinning dynamics; evaporation is much slower. Therefore, in Fig. 15 (TBUT = 11.28 s), it appears that tangential flow thinned the tear film dramatically in the first 3 s, and then evaporation kept thinning the tear film slowly in the last 8 s. The linear approximation $I \propto h$ still holds and self-quenching does not occur even if TBUT is long. In all the cases, we showed in this manuscript, I outperforms \sqrt{I} when approximating the aqueous layer thickness. This result is different from model results from evaporation-driven TBU models (Braun et al. 2015, 2017; King-Smith et al. 2018), in which fluorescein quenching occurs and \sqrt{I} approximates h better than does I . Our model shows that in rapid thinning, if the TBUT is less than 4 s, for $0.1 \leq f_0 \leq 2$ (i.e., $0.02\% \leq f'_0 \leq 0.4\%$), I can approximate h during rapid thinning. Figure 12 is one example. If a subject is suspected to have rapid thinning, then a dilute f_0 can provide a better estimation to the tear film thickness.

As illustrated in Fig. 12, evaporation changes fluorescein concentration which complicates the relationship between the intensity and the thickness via Eq. (11), and thus results in errors in the estimation of h . Therefore, for the best approximation, a different initial FL concentration is required for different TBUT. Figure 17 summarizes this result. For a circular-shaped spot TBU, when TBUT is less than 3 s, $f_0 = 0.3$ ($f'_0 = 0.06\%$) corresponds to the best estimation to the tear film thickness. When TBUT is greater than 4 s, $f_0 = 0.7$ ($f'_0 = 0.14\%$) returns the smallest error. The best choice for initial FL concentration depends on the parameters we choose in this model, such as $(\Delta\sigma)_0$ and the initial thickness h_0 ; as a result, optimal values may vary from case to case.

The reasons for recommending slightly dilute values of the initial FL concentration f_0 can be summarized from Figs. 15 and 16. When f_0 is too small, the fluorescein distribution causes a spurious maximum of intensity to appear for longer TBU times; this spurious maximum came from the absorptance term [the numerator of Eq. (11), see Fig. 16c]. In the case of Fig. 15, this occurred with $f_0 = 0.1$. But for moderate values such as $f_0 = 0.7$, TBU at longer times resulted a lower efficiency $[1/(1 + f^2)]$, see Fig. 16b] in the TBU region due to larger f there. The lowered efficiency counteracts the spurious maximum in intensity from local maximum in f , giving an intensity distribution that closely matches the thickness distribution (Fig. 16d). When f_0 is too large for this kind of TBU, then I is relatively insensitive to changes in the thickness; this is shown in Fig. 11.

FL intensity can be used for estimation of both the tear film thickness and the osmolarity in evaporative dry eye (Braun et al. 2015). The simplest estimation for osmolarity is based on the assumption of conservation of salt ions for flat film, namely $c(r)h(r) = \text{constant}$ (Braun 2012). In rapid thinning, the mass distribution of salt ions is proportional to the tear film thickness as shown in Fig. 8; this is due to changes in thickness for that case. Osmolarity is better assumed to be constant rather than estimated by FL intensity in rapid thinning.

6 Conclusion and Future Work

In this work, we studied the FL imaging in rapid tear thinning by simulating the tear film thinning and solute transport in rapid TBU. The model generates a very strong tangential flow that thins the aqueous layer dramatically in 1 s. Evaporation helps thin the tear film and concentrates concentration over the tear/glob interface. Diffusion flow and advection flow are resulted from the non-uniform distribution of the solutes concentration and the deformed tear film surface. Due to the short TBUT in rapid thinning, if a dilute initial FL is applied, the solutes concentration can be considered as a constant. The computed FL intensity can linearly represent tear film thickness. Initial FL with a concentration higher than f_{cr} will lead to a nonlinear relationship between f and h , which should be avoided when visualizing tear thinning. If TBUT is longer than 4 s, the mechanism becomes complicated; the tangential flow dominates the thinning at beginning, but at later time evaporation becomes more important. The advection and diffusion flow causes variation in the mass distribution of solutes. Initial

FL in the dilute regime and near the critical concentration will better approximate the tear film thickness according to our model.

Our glob models have focused on circular spots and long streaks of TBU. However, in most subjects, rapid TBU may occur in various irregular shapes. Extending the model to two dimensions will make our model more versatile for comparison with experimental results. Besides that, most rapid thinning we observed occurs very rapidly after a full blink, and typically an upward flow exists (Berger and Corrsin 1974; Owens and Phillips 2001; King-Smith et al. 2009). The overall upward flow should be implemented by modifying our boundary conditions.

The models can be further validated by fitting the *in vivo* experimental data by systematically varying the parameters in our models (i.e., parameter identification). Using recent experimental methods to estimate the initial fluorescein concentration can help make this possible, and it may be possible to systematically estimate the osmolarity from fluorescence imaging. It is possible to estimate the initial fluorescein concentration from the inferior meniscus at the beginning of the interblink (Wu et al. 2015); our results suggest optimal values at which to aim, and in principle such experimental estimates could be used to try to approximate those initial values.

Simultaneous imaging of the tear film aqueous and lipid layers is a very valuable direction for future experimental work (King-Smith et al. 2013b, 2018). Developing mathematical models in parallel that include both aqueous and lipid layers is desirable as well (Bruna and Breward 2014; Peng et al. 2014; Stapf et al. 2017).

Acknowledgements This work is funded by NSF Grant 1412085 (Braun), NIH Grant 1R01EY021794 (Begley), and NEI Grant R01EY017951 (King-Smith).

Appendix

A Flow and Solute Transport Dimensional Model

This section gives a detailed derivation in Cartesian coordinates which is applicable to streak TBU.

The following governing equations enforce the conservation of mass of water, momentum and mass of solutes (osmolarity c and concentration of fluorescein f) within the aqueous layer. They apply on $0 < x' < X'_L$ and $0 < z' < h'(x', t')$.

$$\nabla' \cdot \mathbf{u}' = 0, \quad (20)$$

$$\rho (\partial_{t'} \mathbf{u}' + \mathbf{u}' \cdot \nabla' \mathbf{u}') = -\nabla' p' + \mu \nabla'^2 \mathbf{u}', \quad (21)$$

$$\partial_{t'} c' + \nabla' \cdot (\mathbf{u}' c') = D_o \nabla'^2 c', \quad \text{and} \quad \partial_{t'} f' + \nabla' \cdot (\mathbf{u}' f') = D_f \nabla'^2 f'. \quad (22)$$

The aqueous/cornea interface is located at $z' = 0$ and $0 < x' < X'_L$. This is assumed to be a no-slip surface; we assume that there is osmotic flow across a semipermeable membrane and it is proportional to the concentration difference across the boundary:

$$u'_x = 0, \quad \text{and} \quad u'_z = P_0 V_W (c' - c_o). \quad (23)$$

The permeability of the membrane is P_o , the molar volume is V_W , and the isotonic concentration is c_0 . For osmolarity and fluorescein, we assume that the advective fluxes balance the diffusive fluxes at the corneal surface.

$$D_o \partial_{z'} c' - u'_z c' = 0, \quad \text{and} \quad D_f \partial_{z'} f' - u'_z f' = 0 \tag{24}$$

On the free surface of the tear film, $z' = h'$ for $0 < x' < X'_L$. The kinematic boundary condition implies that evaporative flux is the only flux that thins the tear film,

$$J' = \rho(\mathbf{u}'(x', h') - \mathbf{u}'_I) \cdot \mathbf{n}. \tag{25}$$

Here, $\mathbf{u}'(x', h')$ is the fluid velocity evaluated at the free surface, \mathbf{u}'_I is the interface velocity, and $\mathbf{n} = \frac{(-\partial_{x'} h', 1)}{(1+(\partial_{x'} h')^2)^{1/2}}$ is the unit normal vector to the interface. The stress balance in the normal direction to the interface is as follows:

$$-p'_v - \mathbf{n} \cdot \mathbf{T} \cdot \mathbf{n} = \sigma_0 \nabla' \cdot \mathbf{n} - \frac{A'}{h'^3}. \tag{26}$$

The Newtonian stress tensor is $\mathbf{T} = -p' \mathbf{I} + \mu(\nabla' \mathbf{u}' + \nabla' \mathbf{u}'^T)$. We enforce no flux of solutes across the tear film surface ($0 < x' < X'_L$ and $z' = h'$) via

$$D_o \mathbf{n} \cdot \nabla' c' - \mathbf{n} \cdot (\mathbf{u}' - \mathbf{u}'_I) c' = 0. \tag{27}$$

Here, D_o is the diffusivity of osmolarity in water, which is assumed to be that of salts in water (Riquelme et al. 2007). From Eq. (25), the equation above may be written

$$D_o \mathbf{n} \cdot \nabla' c' - \frac{J'}{\rho} c' = 0. \tag{28}$$

Similar to osmolarity, no flux of fluorescein is enforced by

$$D_f \mathbf{n} \cdot \nabla' f' - \frac{J'}{\rho} f' = 0. \tag{29}$$

The model includes a glob on the tear film surface $z' = h'(x', t')$ as a tangentially immobile aqueous/glob interface with a higher concentration of lipid on $0 < x' < X'_I$; the glob is assumed to have a fixed size and a fixed lipid concentration. The aqueous/air interface on $X'_I \leq x' \leq X'_L$ is mobile, and conservation of mass for the insoluble polar lipid is governed by the following transport equation there.

$$\Gamma' = \Gamma_0 \quad \text{in} \quad [0, X'_I], \quad \text{and} \quad \partial_{t'} \Gamma' + \nabla'_s \cdot (\Gamma' \mathbf{u}') = D_s \nabla_s'^2 \Gamma' \quad \text{in} \quad [X'_I, X'_L]. \tag{30}$$

The surface Laplacian is defined as $\nabla_s' = (I - \mathbf{n} \cdot \mathbf{n}) \nabla'$. The corresponding definition in tensor notation can be found in (Slattery et al. 2007). While surfactant mass is conserved individually within the glob and in the mobile region outside the glob, when we put them together on the tear film, the glob will act as a source of surfactant

for the mobile region; we believe that this caricature is value for understanding the tear film dynamics driven by globs.

The tangential stress boundary condition under the glob and outside the glob is different because of our assumptions about the glob. Under the glob, $z' = h'$ and on $(0, X'_I)$, the no-slip boundary condition is assumed to hold (which replaces the tangential stress boundary condition), while outside of the glob $z' = h'$, and on (X'_I, X'_L) , tangential stress balance is enforced:

$$u'_{x'} = 0 \quad \text{in} \quad (0, X'_I), \quad (31)$$

and

$$\mathbf{t} \cdot \mathbf{T} \cdot \mathbf{n} = \partial_S \sigma = \mathbf{t} \cdot \nabla' \sigma = \mathbf{t} \cdot \nabla' [\sigma_0 - (\partial_{\Gamma} \sigma)_0 (\Gamma' - \Gamma_0)] \quad \text{in} \quad (X'_I, X'_L). \quad (32)$$

The unit tangent vector to the interface is $\mathbf{t} = \frac{(1, \partial_{x'} h')}{(1 + (\partial_{x'} h')^2)^{1/2}}$.

B Dimensionless Models and Model Reduction

The model in Cartesian coordinates and one independent space variable represents the glob in a streak shape. In the independent variables (x', z') , the corresponding fluid velocity is $(u'_{x'}, u'_{z'})$. Similarly, for the axisymmetric spot model, in the cylindrical coordinates (r', z') , the fluid velocity is $(u'_{r'}, u'_{z'})$.

B.1 Scalings

We simplify the streak glob model and spot glob model using the following scalings. The value of dimensional parameters used for scaling can be found in Table 2.

$$\begin{aligned} x' &= \ell x, \quad z' = d' z, \quad t' = \frac{\ell}{U} t, \quad h' = d' h, \quad u'_{x'} = U u_x, \quad u'_{z'} = \epsilon U u_z, \quad (33) \\ p' &= \frac{\mu U}{\ell \epsilon^2} p, \quad J' = \epsilon \rho U J, \quad \Gamma' = \Gamma_0 \Gamma, \quad c' = c_o c, \quad f' = f_{\text{cr}} f. \quad (34) \end{aligned}$$

B.2 Reduced Dimensionless Streak Model

We use the scalings in Sect. B.1 for the non-dimensionalization of our systems (in Sect. A). Dropping all the terms in the dimensionless equations, except the leading-order terms, we reduce our systems to be a simpler problem. The following are the reduced dimensionless equations for the streak TBU model.

The reduced governing equations inside the aqueous layer $(0 < z < h, 0 < x < X_L)$, which enforce the conservation of mass of water, momentum and mass of solutes

Table 2 Dimensional parameters used in this paper

Parameter	Description	Value	References
d'	Tear film thickness	$3.5 \mu\text{m}$	Braun and King-Smith (2007)
ρ	Density	$10^3 \text{ kg} \cdot \text{m}^{-3}$	Water
μ	Viscosity	$1.3 \times 10^{-3} \text{ Pa} \cdot \text{s}$	Tiffany (1991)
V_w	Molar volume of water	$1.8 \times 10^{-5} \text{ m}^3 \cdot \text{mol}^{-1}$	Water
P_o	Permeability of cornea	$12.1 \times 10^{-6} \text{ m/s}$	Braun et al. (2015)
D_s	Surface diffusion coefficient	$3 \times 10^{-8} \text{ m}^2/\text{s}$	Sakata and Berg (1969)
D_f	Diffusivity of fluorescein	$0.39 \times 10^{-9} \text{ m}^2/\text{s}$	Casalini et al. (2011)
D_o	Diffusivity of salt	$1.6 \times 10^{-9} \text{ m}^2/\text{s}$	Riquelme et al. (2007)
ϵ_f	Naperian extinction coefficient	$1.75 \times 10^7 \text{ m}^{-1} \text{ M}^{-1}$	Mota et al. (1991)
A^*	Hamaker constant	$6\pi \times 3.5 \times 10^{-19} \text{ Pa} \cdot \text{m}^3$	Winter et al. (2010)
c_o	Isotonic osmolarity	$3 \times 10^{-4} \text{ mol/m}^3$	Lemp et al. (2011)
σ_0	Surface tension	$0.045 \text{ N} \cdot \text{m}^{-1}$	Nagyová and Tiffany (1999)
$(\partial_\Gamma \sigma)_0$	Composition dependence	0.01 N/m	Aydemir et al. (2010)
$(\Delta \sigma)_0$	Change in surface tension	10^{-4} N/m	$\Gamma_0(\partial_\Gamma \sigma)_0$
ℓ	Characteristic length	0.0742 mm	$[\sigma_0/(\Delta \sigma)_0]^{1/2} d'$
U	Characteristic velocity	0.0036 m/s	$[(\Delta \sigma)_0]^{3/2}/[\mu(\sigma_0)^{1/2}]$
t_s	Timescale	0.0205 s	$\sigma_0 d\mu/[(\Delta \sigma)_0]^2$

are:

$$\partial_x u_x + \partial_z u_z = 0, \tag{35}$$

$$\partial_{zz} u_x - \partial_x p = 0, \quad \partial_z p = 0, \tag{36}$$

$$\partial_t c + u_x \partial_x c + u_z \partial_z c = \text{Pe}_c^{-1} (\partial_{xx} c + \epsilon^{-2} \partial_{zz} c), \quad \text{and} \tag{37}$$

$$\partial_t f + u_x \partial_x f + u_z \partial_z f = \text{Pe}_f^{-1} (\partial_{xx} f + \epsilon^{-2} \partial_{zz} f). \tag{38}$$

At the aqueous/cornea interface $z = 0$ and $0 < x < X_L$, we have no-slip and water permeability boundary conditions,

$$u_x = 0, \quad u_z = \text{P}_c (c - 1). \tag{39}$$

We also assume there is no fluxes of solutes:

$$\epsilon^{-2} \text{Pe}_c^{-1} \partial_z c = u_z c \quad \text{and} \quad \epsilon^{-2} \text{Pe}_f^{-1} \partial_z f = u_z f. \tag{40}$$

Across the domain $[0, X_L]$ at tear film surface $z = h(x, t)$, our kinematic boundary condition, tangential stress boundary condition and conservation of mass solutes result

in the following dimensionless form,

$$\partial_t h + u_x \partial_x h - u_z = -J(x), \quad (41)$$

$$p = -S \partial_{xx} h - Ah^{-3}, \quad (42)$$

$$\partial_z c = \epsilon^2 (\text{Pe}_c Jc + \partial_x h \partial_x c) \quad \text{and} \quad \partial_z f = \epsilon^2 (\text{Pe}_f Jf + \partial_x h \partial_x f). \quad (43)$$

Boundary conditions for the tangential immobility and fixed lipid concentration at the aqueous/glob interface $0 \leq x \leq X_I$ become

$$u_x = 0 \quad \text{and} \quad \Gamma = 1. \quad (44)$$

At the aqueous/air interface $[X_I, X_L]$, conservation of surfactant is now

$$\partial_z u_x = -M \partial_x \Gamma \quad \text{and} \quad \partial_t \Gamma + \partial_x (u_s \Gamma) = \text{Pe}_s^{-1} \partial_x^2 \Gamma. \quad (45)$$

Here, \mathbf{u}'_s is the surface velocity and is defined as $\mathbf{u}'_s = \nabla'_s \mathbf{u}$. The dimensionless surface velocity is

$$\mathbf{u}_s = \frac{1}{1 + \epsilon^2 (\partial_x h)^2} (u + \epsilon^2 u_z (\partial_x h)^2, \epsilon^3 u_z (\partial_x h)^2 + \epsilon u \partial_x h) \quad (46)$$

If only keep the leading order, $\mathbf{u}_s = (u, 0)$. To make a difference between \mathbf{u}_s and u , we denote the surface velocity in the x direction using u_s .

B.3 Reduction of the PDE System

The model in preceding section can be reduced to the lubrication approximation in the following ways. The process are similar for streak model and spot model. We show example in the streak case.

Equation (36) shows that $p = p(x, t)$, which results in

$$u_x = \frac{\partial_x p}{2} z^2 + C(x, t)z + D(x, t). \quad (47)$$

The boundary conditions on corneal surface and tear film surface for u are:

$$u_x = 0 \quad \text{at} \quad z = 0, \quad u(1 - B(x)) + (\partial_z u_x + M \partial_x \Gamma)B(x) = 0 \quad \text{at} \quad z = h, \quad (48)$$

which implies that

$$u_x = \frac{\partial_x p}{2} z^2 + C(x, t)z, \quad C(x, t) = \frac{-\frac{\partial_x p}{2} h [h(1 - B) + 2B] - MB \partial_x \Gamma}{h(1 - B) + B}. \quad (49)$$

Integrating Eq. (35) in z and combined with Leibnitz rule, we have the following:

$$\partial_x h u_x(x, h, t) - u_z(x, h, t) = \partial_x (h \bar{u}) - \text{Pe}_c (c(x, 0, t) - 1), \quad (50)$$

where $\bar{u}(x, t) = \frac{1}{h} \int_0^h u_x(x, z, t) dz$ is the depth averaged velocity along the film. Substituting it into Eq. (41), we arrive at

$$\partial_t h = -\partial_x(h\bar{u}) + \text{Pe}_c(c(x, 0, t) - 1) - J(x). \tag{51}$$

Solving for c and f are similar (Jensen and Grotberg 1993); here we only illustrate the process for c . Assume c has the following expansion,

$$c(x, z, t) = c_0(x, z, t) + \epsilon^2 c_1(x, z, t) + \dots \tag{52}$$

Substitution into Eq. (38) and collecting terms, we obtain the leading-order equation

$$\partial_{zz} c_0 = 0. \tag{53}$$

The leading-order term from either boundary is $\partial_z c_0 = 0$; using the boundary conditions results in

$$c_0 = c_0(x, t). \tag{54}$$

We then further collect terms corresponding to $O(\epsilon^2)$ in (38) to obtain

$$\text{Pe}_c(\partial_t c_0 + u_x \partial_x c_0) - \partial_{xx} c_0 = \partial_{zz} c_1. \tag{55}$$

Integrating Eq. (55) with respect to z over $(0, h)$, we obtain

$$\text{Pe}_c h(\partial_t c_0 + \bar{u} \partial_x c_0) - h \partial_{xx} c_0 = \partial_z c_1(x, h, t) - \partial_z c_1(x, 0, t). \tag{56}$$

The boundary condition at $z = 0$ from Eq. (40) and $z = h$ from Eq. (43) becomes, at the first nonzero order,

$$\partial_z c_1(x, 0, t) = \text{Pe}_c u_z(x, 0, t) c_0, \quad \text{and} \quad \partial_z c_1(x, h, t) = \text{Pe}_c J c_0 + \partial_x h \partial_x c_0. \tag{57}$$

Using these conditions to eliminate c_1 in Eq. (56) results in, after dropping the subscript,

$$h(\partial_t c + \bar{u} \partial_x c) = \text{Pe}_c^{-1} \partial_{xx} c + Jc + \partial_x h \partial_x c - \text{Pe}_c(c - 1)c. \tag{58}$$

Proceeding in a similar way with fluorescein, we obtain

$$h(\partial_t f + \bar{u} \partial_x f) = \text{Pe}_f^{-1} \partial_{xx} f + Jf + \partial_x h \partial_x f - \text{Pe}_c(c - 1)f. \tag{59}$$

Now, in summary, we have the following five PDEs.

$$\partial_t h = -\partial_x(h\bar{u}) + \text{Pe}_c(c - 1) - J, \tag{60}$$

$$p = -\partial_{xx} h - Ah^{-3}, \tag{61}$$

$$\partial_t \Gamma = [\text{Pe}_s^{-1} \partial_x^2 \Gamma - \partial_x(u_s \Gamma)]B(x), \tag{62}$$

$$h(\partial_t c + \bar{u} \partial_x c) = \text{Pe}_c^{-1} \partial_{xx} c + Jc + \partial_x h \partial_x c - \text{Pe}_c(c - 1)c, \tag{63}$$

$$h(\partial_t f + \bar{u} \partial_x f) = \text{Pe}_f^{-1} \partial_{xx} f + Jf + \partial_x h \partial_x f - \text{Pe}_c(c - 1)f. \tag{64}$$

Here,

$$\bar{u} = \frac{-\frac{1}{3}\partial_x p h^2 [\frac{1}{4}(1-B)h + B] - \frac{1}{2}\partial_x \Gamma B h}{(1-B)(\beta + h) + B}, \quad (65)$$

$$u_s = \frac{-B [(h^2/2)\partial_x p + h\partial_x \Gamma]}{(1-B)h + B}. \quad (66)$$

B.4 Streak Boundary and Initial Conditions

As in the spot problem, we apply symmetry at the origin and no-flux conditions at the other end of the domain. At the center of glob $x = 0$, the boundary conditions enforce symmetry and thus no flux via

$$\partial_x h = \partial_x p = \partial_x \Gamma = \partial_x c = \partial_x f = 0. \quad (67)$$

We enforce no-flux conditions on h , p , Γ , c and f at $x = X_L$, and these end up being Eq. (67) applied at the other end.

The initial conditions are again spatially uniform (except for Γ); on $0 \leq x \leq X_L$,

$$h(x, 0) = c(x, 0) = f(x, 0) = 1, \quad \text{and} \quad p(x, 0) = -A. \quad (68)$$

We assume that the glob has high surfactant concentration and the mobile tear/air interface outside of it has a lower concentration initially. From our scalings, $\Gamma = 1$ under the glob and $\Gamma = 0.1$ outside the glob. Using the transition function $B(x)$, the initial condition for Γ is then

$$\Gamma(r, 0) = 1 \cdot [1 - B(x)] + 0.1 \cdot B(x). \quad (69)$$

B.5 Reduced Dimensionless Spot Model

The derivation for spot model in axisymmetric cylindrical coordinate is similar to the streak model in one dimension. In this subsection, we will just list the dimensionless model with only leading-order terms.

Inside the aqueous layer $0 < z < h$, $0 < r < R_L$, the conservation laws of mass of water, momentum and mass of solutes are

$$\frac{1}{r} \frac{\partial}{\partial r} (r u_r) + \frac{\partial u_z}{\partial z} = 0, \quad (70)$$

$$\partial_r p = -\partial_z^2 u_r \quad \& \quad \partial_z p = 0, \quad (71)$$

$$\partial_t c + u_r \partial_r c + u_z \partial_z c = \text{Pe}_c^{-1} \left[\frac{1}{r} \partial_r (r \partial_r c) + \epsilon^{-2} \partial_z^2 c \right], \quad (72)$$

$$\partial_t f + u_r \partial_r f + u_z \partial_z f = \text{Pe}_f^{-1} \left[\frac{1}{r} \partial_r (r \partial_r f) + \epsilon^{-2} \partial_z^2 f \right]. \quad (73)$$

At corneal surface $z = 0, 0 < r < R_L$, the no-slip boundary conditions and osmotic flow through semipermeable membrane are defined as follows:

$$u_r(r, 0, t) = 0 \quad \text{and} \quad u_z(r, 0, t) = P_c(c - 1). \tag{74}$$

In addition, there are two more conditions for non-flux of solutes,

$$\epsilon^{-2}Pe_c^{-1}\partial_z c = u_z c \quad \text{and} \quad \epsilon^{-2}Pe_f^{-1}\partial_z f = u_z f. \tag{75}$$

At the tear film surface ($z = h, 0 < r < R_L$), the kinematic boundary condition and normal stress balance are simplified to be

$$\partial_t h + u_r \partial_r h - u_z = -J, \quad \text{and} \quad p - p_v = -S \frac{1}{r} \partial_r (r \partial_r h) - Ah^{-3}. \tag{76}$$

The equations of no fluxes of solutes are

$$\partial_z c = \epsilon^2 [Pe_c Jc + \partial_r h \partial_r c], \quad \text{and} \quad \partial_z f = \epsilon^2 [Pe_f Jf + \partial_r h \partial_r f]. \tag{77}$$

At the aqueous/glob interface, $z = h$ and $0 < r < R_I$, the no-slip boundary condition and a fixed surfactant concentration are as follows:

$$u_r = 0, \quad \Gamma = 1. \tag{78}$$

At the aqueous/air interface, $z = h$ and $R_I < r < R_L$, the boundary condition for Γ reduced to be

$$\partial_z u_r = -M \partial_r \Gamma, \quad \text{and} \quad \partial_t \Gamma = Pe_s^{-1} \left[\frac{1}{r} \partial_r (r \partial_r \Gamma) \right] - \frac{1}{r} \partial_r (r \Gamma u_r). \tag{79}$$

The boundary and initial conditions are given in the text.

C Other Evaporation Fluxes

Besides the evaporation fluxes in Eq. (10), three other fluxes also have been used here.

Case (a): If lipid with higher concentration provides a better barrier to evaporation, we may assume that there is no evaporation over the glob. The edge of the glob corresponds to the highest evaporation rate v_{\max} due to the abnormal decreasing of concentration of lipid. The aqueous/air interface corresponds to the uniform evaporation rate v_{\min} for the uniform distributed lipid concentration.

$$J(r) = a(1 - v_{\min})(r - R_I)e^{-\frac{(r-R_I)^2}{2R_W^2}} + v_{\min} \tanh\left(\frac{r - R_I}{R_W}\right), \tag{80}$$

where the constant a is given by

$$a = \frac{e^{1/2}[v_{\max} - v_{\min} \tanh(1)]}{(1 - v_{\min})R_W}. \quad (81)$$

Case (b): If the higher concentration of lipid results in a poor barrier to evaporation, we let the evaporation rate be low on the glob and high at the aqueous/air interface:

$$J(r) = v_{\min} [1 - B(r)] + v_{\max} B(r). \quad (82)$$

Case (c): The different compositions of glob are assumed to have no effect on evaporation; in that case, the evaporation rate is uniform across the entire domain,

$$J(r) = v_{\max}. \quad (83)$$

References

- Amparo F, Jin Y, Hamrah P, Schaumberg DA, Dana R (2014) What is the value of incorporating tear osmolarity measurement in assessing patient response to therapy in dry eye disease? *Am J Ophthalmol* 157(1):69–77
- Aydemir E, Breward CJW, Witelski TP (2010) The effect of polar lipids on tear film dynamics. *Bull Math Biol* 73:1171–1201
- Begley C, Simpson T, Liu H, Salvo E, Wu Z, Bradley A, Situ P (2013a) Quantitative analysis of tear film fluorescence and discomfort during tear film instability and thinningsensory responses during tear film breakup and thinning. *Invest Ophthalmol Vis Sci* 54(4):2645–2653
- Begley CG, Himebaugh N, Renner D, Liu H, Chalmers R, Simpson T, Varikooty J (2006) Tear breakup dynamics: a technique for quantifying tear film instability. *Optom Vis Sci* 83(1):15–21
- Begley CG, Simpson T, Liu H, Salvo E, Wu Z, Bradley A, Situ P (2013b) Quantitative analysis of tear film fluorescence and discomfort during tear film instability and thinning. *Invest Ophthalmol Vis Sci* 54:2645–2653
- Benedetto DA, Clinch TE, Laibson PR (1986) In vivo observations of tear dynamics using fluorophotometry. *Arch Ophthalmol* 102:410–412
- Berger RE, Corsin S (1974) A surface tension gradient mechanism for driving the pre-corneal tear film after a blink. *J Biomech* 7:225–238
- Bitton E, Lovasik JV (1998) Longitudinal analysis of precorneal tear film rupture patterns. In: Sullivan DA, Dartt DA, Meneray MA (eds) *Advances in experimental medicine and biology, Lacrimal gland, tear film, and dry eye syndromes 2*, Springer, Berlin., vol 438, pp 381–389
- Braun RJ (2012) Dynamics of the tear film. *Annu Rev Fluid Mech* 44:267–297
- Braun RJ, Fitt AD (2003) Modeling the drainage of the precorneal tear film after a blink. *Math Med Biol* 20:1–28
- Braun RJ, King-Smith PE (2007) Model problems for the tear film in a blink cycle: single equation models. *J Fluid Mech* 586:465–490
- Braun RJ, Usha R, McFadden GB, Driscoll TA, Cook LP, King-Smith PE (2012) Thin film dynamics on a prolate spheroid with application to the cornea. *J Eng Math* 73:121–138
- Braun RJ, Gewecke N, Begley CG, King-Smith PE, Siddique JI (2014) A model for tear film thinning with osmolarity and fluorescein. *Invest Ophthalmol Vis Sci* 55:1133–1142
- Braun RJ, King-Smith PE, Begley CG, Li L, Gewecke NR (2015) Dynamics and function of the tear film in relation to the blink cycle. *Prog Retin Eye Res* 45:132–164
- Braun RJ, Driscoll TA, Begley CG, King-Smith PE, Siddique JI (2017) On tear film breakup (TBU): dynamics and imaging. *Math Med Biol* 45:1–36
- Bron A, Tiffany J, Gouveia S, Yokoi N, Voon L (2004) Functional aspects of the tear film lipid layer. *Exp Eye Res* 78:347–360
- Bron A, Argüeso P, Irkec M, Bright FV (2015) Clinical staining of the ocular surface: mechanisms and interpretations. *Prog Ret Eye Res* 78:36–61

- Bruna M, Breward CJW (2014) The influence of nonpolar lipids on tear film dynamics. *J Fluid Mech* 746:565–605
- Casalini T, Salvalaglio M, Perale G, Masi M, Cavallotti C (2011) Diffusion and aggregation of sodium fluorescein in aqueous solutions. *J Phys Chem B* 115:12,896–12,904
- Craig JP, Tomlinson A (1997) Importance of the lipid layer in human tear film stability and evaporation. *Optom Vis Sci* 74:8–13
- Craig JP, Nichols KK, Akpek EK, Caffery B, Dua HS, Joo CK, Liu Z, Nelson JD, Nichols JJ, Tsubota K et al (2017) TFOS DEWS-II definition and classification report. *Ocul Surf* 15(3):276283
- Craster RV, Matar OK (2009) Dynamics and stability of thin liquid films. *Rev Mod Phys* 81:1131–1198
- Efron N (2013) Putting vital stains in context. *Clin Exp Optom* 96(4):400–421
- Farris RL (1994) Tear osmolarity—a new gold standard? In: *Lacrimal Gland, Tear Film, and Dry Eye Syndromes*, Springer, Berlin, pp 495–503
- Gilbard JP, Farris RL, Santamaria J (1978) Osmolarity of tear microvolumes in keratoconjunctivitis sicca. *Arch Ophthalmol* 96:677–681
- Gipson IK (2004) Distribution of mucins at the ocular surface. *Exp Eye Res* 78:379–388
- Govindarajan B, Gipson I (2010) Membrane-tethered mucins have multiple functions on the ocular surface. *Exp Eye Res* 90:655–693
- Heryudono A, Braun RJ, Driscoll TA, Cook LP, Maki KL, King-Smith PE (2007) Single-equation models for the tear film in a blink cycle: realistic lid motion. *Math Med Biol* 24:347–377
- Holly F (1973) Formation and rupture of the tear film. *Exp Eye Res* 15:515–525
- Israelachvili JN (2011) *Intermolecular and surface forces*. Academic Press, San Diego
- Jensen OE, Grotberg JB (1993) The spreading of heat or soluble surfactant along a thin liquid film. *Phys Fluids A* 75:58–68
- Johnson ME, Murphy PJ (2004) Changes in the tear film and ocular surface from dry eye syndrome. *Prog Ret Eye Res* 23:449–474
- Jones MB, Please CP, McElwain DLS, Fulford GR, Roberts AP, Collins MJ (2005) Dynamics of tear film deposition and drainage. *Math Med Bio* 22:265–288
- Jones MB, McElwain DLS, Fulford GR, Collins MJ, Roberts AP (2006) The effect of the lipid layer on tear film behavior. *Bull Math Biol* 68:1355–1381
- Kamao T, Yamaguchi M, Kawasaki S, Mizoue S, Shiraishi A, Ohashi Y (2011) Screening for dry eye with newly developed ocular surface thermographer. *Am J Ophthalmol* 151:782–791 e1
- King-Smith PE, Fink BA, Hill RM, Koelling KW, Tiffany JM (2004) The thickness of the tear film. *Curr Eye Res* 29:357–368
- King-Smith PE, Nichols JJ, Nichols KK, Fink BA, Braun RJ (2008) Contributions of evaporation and other mechanisms to tear film thinning and breakup. *Optom Vis Sci* 85:623–630
- King-Smith PE, Fink BA, Nichols JJ, Nichols KK, Braun RJ, McFadden GB (2009) The contribution of lipid layer movement to tear film thinning and breakup. *Invest Ophthalmol Visual Sci* 50:2747–2756
- King-Smith PE, Hinel EA, Nichols JJ (2010) Application of a novel interferometric method to investigate the relation between lipid layer thickness and tear film thinning. *Invest Ophthalmol Vis Sci* 51:2418–2423
- King-Smith PE, Nichols JJ, Braun RJ, Nichols KK (2011) High resolution microscopy of the lipid layer of the tear film. *Ocul Surf* 9(4):197–211
- King-Smith PE, Ramamoorthy P, Braun RJ, Nichols JJ (2013a) Tear film images and breakup analyzed using fluorescent quenching. *Invest Ophthalmol Vis Sci* 54:6003–6011
- King-Smith PE, Reuter KS, Braun RJ, Nichols JJ, Nichols KK (2013b) Tear film breakup and structure studied by simultaneous video recording of fluorescence and tear film lipid layer, TFLL, images. *Invest Ophthalmol Vis Sci* 54:4900–4909
- King-Smith PE, Begley CG, Braun RJ (2018) Mechanisms, imaging and structure of tear film breakup. *Ocul Surf* 16:4–30
- Leiske DL, Miller CE, Rosenfeld L, Cerretani C, Ayzner A, Lin B, Meron M, Senchyna M, Ketelson HA, Meadows D, Srinivasan S, Jones L, Radke CJ, Toney MF, Fuller GG (2012) Molecular structure of interfacial human meibum films. *Langmuir* 28:11,858–11,865
- Lemp MA (2007) The definition and classification of dry eye disease: report of the definition and classification subcommittee of the international dry eye workshop. *Ocul Surf* 5:75–92
- Lemp MA, Baudouin C, Baum J, Dogru M, Foulks GN, Kinoshita S, Laibson P, McCulley J, Murube J, Pflugfelder SC (2007) The definition and classification of dry eye disease: report of the definition and classification subcommittee of the international dry eye workshop. *Ocul Surf* 5(2):75–92

- Lemp MA, Bron AJ, Baudoin C, Benitez Del Castillo JM, Geffen D, Tauber J, Foulks GN, Pepose JS, Sullivan BD (2011) Tear osmolarity in the diagnosis and management of dry eye disease. *Am J Ophthalmol* 151:792–798
- Li DQ, Luo L, Chen Z, Kim HS, Song XJ, Pflugfelder SC (2006) JNK and ERK MAP kinases mediate induction of IL-1 β , TNF- α and IL-8 following hyperosmolar stress in human limbal epithelial cells. *Exp Eye Res* 82(4):588–596
- Li L, Braun RJ, Maki KL, Henshaw WD, King-Smith PE (2014) Tear film dynamics with evaporation, wetting and time-dependent flux boundary condition on an eye-shaped domain. *Phys Fluids* 26(052):101
- Li L, Braun RJ, Henshaw WD, King-Smith PE (2017) Computed flow and fluorescence over the ocular surface. *Math Med Biol Adv Access*. <https://doi.org/10.1093/imammb/dqx011:1-33>
- Liu H, Begley CG, Chalmers R, Wilson G, Srinivas SP, Wilkinson JA (2006) Temporal progression and spatial repeatability of tear breakup. *Optom Vis Sci* 83:723–730
- Liu H, Begley CG, Chen M, Bradley A, Bonanno J, McNamara NA, Nelson JD, Simpson T (2009) A link between tear instability and hyperosmolarity in dry eye. *Invest Ophthalmol Vis Sci* 50:3671–3679
- Maki KL, Braun RJ, Henshaw WD, King-Smith PE (2010a) Tear film dynamics on an eye-shaped domain I. Pressure boundary conditions. *Math Med Biol* 27:227–254
- Maki KL, Braun RJ, Ucciferro P, Henshaw WD, King-Smith PE (2010b) Tear film dynamics on an eye-shaped domain. Part 2. Flux boundary conditions. *J Fluid Mech* 647:361–390
- McCulley J, Shine W (1997) A compositional based model for the tear film lipid layer. *Trans Am Ophthalmol Soc* 95:79
- Mcmonnies CW (2018) Tear instability importance, mechanisms, validity and reliability of assessment. *J Optom* 11(4):203–210
- Mertzanis P, Abetz L, Rajagopalan K, Espindle D, Chalmers R, Snyder C, Caffery B, Edrington T, Simpson T, Nelson JD, Begley C (2005) The relative burden of dry eye in patients' lives: comparisons to a U.S. normative sample. *Invest Ophthalmol Vis Sci* 46(1):46–50
- Messmer EM, Bulgen M, Kampik A (2010) Hyperosmolarity of the tear film in dry eye syndrome. *Res Proj Dry Eye Syndr* 45:129–138
- Miljanović B, Dana R, Sullivan DA, Schaumberg DA (2007) Impact of dry eye syndrome on vision-related quality of life. *Am J Ophthalmol* 143(3):409–415
- Miller KL, Polse KA, Radke CJ (2002) Black line formation and the “perched” human tear film. *Curr Eye Res* 25:155–162
- Mishima S, Maurice D (1961) The oily layer of the tear film and evaporation from the corneal surface. *Exp Eye Res* 1:39–45
- Mota MC, Carvalho P, Ramalho J, Leite E (1991) Spectrophotometric analysis of sodium fluorescein aqueous solutions. Determination of molar absorption coefficient. *Int Ophthalmol* 15:321–326
- Nagyová B, Tiffany JM (1999) Components of tears responsible for surface tension. *Curr Eye Res* 19:4–11
- Nelson JD, Craig JP, Akpek EK, Azar DT, Belmonte C, Bron AJ, Clayton JA, Dogru M, Dua HS, Foulks GN (2017) TFOS DEWS-II introduction. *Ocul Surf* 15(3):269–275
- Nichols JJ, Mitchell GL, King-Smith PE (2005) Thinning rate of the precorneal and prelens tear films. *Invest Ophthalmol Vis Sci* 46:2353–2361
- Nichols JJ, King-Smith PE, Hinel EA, Thangavelu M, Nichols KK (2012) The use of fluorescent quenching in studying the contribution of evaporation to tear thinning. *Invest Ophthalmol Vis Sci* 53:5426–5432
- Norn M (1969) Dessication of the precorneal film I. Corneal wetting time. *Acta Ophthalmol* 47(4):865–880
- Norn MS (1979) Semiquantitative interference study of the fatty layer of precorneal film. *Acta Ophthalmol* 57:766–774
- Oron A, Bankoff SG (1999) Dewetting of a heated surface by an evaporating liquid film under conjoining/disjoining pressures. *J Colloid Interface Sci* 218(1):152–166
- Oron A, Davis SH, Bankoff SG (1997) Long-scale evolution of thin liquid films. *Rev Mod Phys* 69:931–980
- Owens H, Phillips J (2001) Spreading of the tears after a blink: velocity and stabilization time in healthy eyes. *Cornea* 20:484–487
- Paananen RO, Rantamäki AH, Holopainen JM (2014) Antieaporative mechanism of wax esters: implications for the function of tear fluid. *Langmuir* 30(20):5897–5902
- Peng CC, Cerretani C, Braun RJ, Radke CJ (2014) Evaporation-driven instability of the precorneal tear film. *Adv Coll Interface Sci* 206:250–264
- Pult H, Tosatti SG, Nicholas SJM, Asfour D, Ebenhoch M, Murphy PJ (2015) Spontaneous blinking from a tribological viewpoint. *Ocul Surf* 13:236–239

- Riquelme R, Lira I, Pérez-López C, Rayas JA, Rodríguez-Vera R (2007) Interferometric measurement of a diffusion coefficient: comparison of two methods and uncertainty analysis. *J Phys D Appl Phys* 40:2769–2776
- Rosenfeld L, Cerretani C, Leiske DL, Toney MF, Radke CJ, Fuller GG (2013) Structural and rheological properties of meibomian lipid. *Invest Ophthalmol Vis Sci* 54:2720–2732
- Sakata E, Berg J (1969) Surface diffusion in monolayers. *Ind Eng Chem Fundam* 8(3):570–573
- Scott JA (1988) A finite element model of heat transport in the human eye. *Phys Med Biol* 33:227–241
- Sebbag L, Park S, Kass PH, Maggs DJ, Attar M, Murphy CJ (2017) Assessment of tear film osmolarity using the TearLab™ osmometer in normal dogs and dogs with keratoconjunctivitis sicca. *Vet Ophthalmol* 20(4):357–364
- Sharma A (1998) Acid-base interactions in the cornea-tear film system: surface chemistry of corneal wetting, cleaning, lubrication, hydration and defense. *J Dispers Sci Technol* 19(6–7):1031–1068
- Sharma A, Khanna R (1998) Pattern formation in unstable thin liquid films. *Phys Rev Lett* 81:3463–3466
- Sharma A, Ruckenstein E (1985) Mechanism of tear film rupture and formation of dry spots on cornea. *J Colloid Interface Sci* 106:12–27
- Sharma A, Ruckenstein E (1986) The role of lipid abnormalities, aqueous and mucus deficiencies in the tear film breakup, and implications for tear substitutes and contact lens tolerance. *J Colloid Interface Sci* 111:456–479
- Siddique JI, Braun RJ (2015) Tear film dynamics with evaporation, osmolarity and surfactant transport. *Appl Math Model* 39:255–269
- Slattery JC, Sagis L, Oh ES (2007) *Interfacial transport phenomena*. Springer, Berlin
- Stahl U, Willcox M, Stapleton F (2012) Osmolality and tear film dynamics. *Clin Exp Ophthalmol* 95(1):3–11
- Stapf M, Braun R, King-Smith P (2017) Duplex tear film evaporation analysis. *Bull Math Biol* 79(12):2814–2846
- Stapleton F, Garrett Q, Chan C, Craig JP (2015) *The epidemiology of dry eye disease*. Dry Eye Springer Berlin Chap 2:21–29
- Su TY, Chang SW, Yang CJ, Chiang HK (2014) Direct observation and validation of fluorescein tear film break-up patterns by using a dual thermal-fluorescent imaging system. *Biomed Opt Express* 5(8):2614–2619
- Szalai E, Berta A, Szekanez Z, Szűcs G, Módos L Jr (2012) Evaluation of tear osmolarity in non-sjögren and sjögren syndrome dry eye patients with the TearLab system. *Cornea* 31(8):867–871
- Tiffany JM (1991) The viscosity of human tears. *Int Ophthalmol* 15:371–376
- Tomlinson A, Khanal S, Ramesh K, Diaper C, McFadyen A (2006) Tear film osmolarity as a referent for dry eye diagnosis. *Invest Ophthalmol Vis Sci* 47:4309–4315
- Trefethen LN (2000) *Spectral methods in MATLAB*. SIAM, Philadelphia
- Versura P, Campos EC (2013) Tearlab® osmolarity system for diagnosing dry eye. *Expert Rev Mol Diagn* 2(13):119–129
- Webber WRS, Jones DP (1986) Continuous fluorophotometric method measuring tear turnover rate in humans and analysis of factors affecting accuracy. *Med Biol Eng Comput* 24:386–392
- Winter KN, Anderson DM, Braun RJ (2010) A model for wetting and evaporation of a post-blink precorneal tear film. *Math Med Biol* 27:211–225
- Wolffsohn JS, Arita R, Chalmers R, Djalilian A, Dogru M, Dumbleton K, Gupta PK, Karpecki P, Lazreg S, Pult H et al (2017) TFOS DEWS-II diagnostic methodology report. *Ocul Surf* 15(3):539–574
- Wong H, Fatt I, Radke C (1996) Deposition and thinning of the human tear film. *J Colloid Interface Sci* 184(1):44–51
- Wu Z, Begley CG, Port N, Bradley A, Braun RJ, King-Smith PE (2015) The effects of increasing ocular surface stimulation on blinking and tear secretion. *Invest Ophthalmol Vis Sci* 56(8):4211–4220
- Yanez-Soto B, Mannis MJ, Schwab I, Li JY, Leonard BC, Abbott NL, Murphy CJ (2014) Interfacial phenomena and the ocular surface. *Ocul Surf* 12:178–201
- Yanez-Soto B, Leonard BC, Raghunathan VK, Abbott NL, Murphy CJ (2015) Effect of stratification on the surface properties of corneal epithelial cells. *Invest Ophthalmol Vis Sci* 56:8340–8348
- Yokoi N, Georgiev GA (2013a) Tear dynamics and dry eye disease. *Ocul Surf Dis*, JP Medical Ltd, London, p 47
- Yokoi N, Georgiev GA (2013b) Tear-film-oriented diagnosis and therapy for dry eye. *Dry eye syndrome: basic and clinical perspectives*. Future Medicine Ltd, London, pp 96–108

- Yokoi N, Georgiev GA, Kato H, Komuro A, Sonomura Y, Sotozono C, Tsubota K, Kinoshita S (2017) Classification of fluorescein breakup patterns: A novel method of differential diagnosis for dry eye. *Am J Ophthalmol* 180:72–85
- Zhang L, Matar OK, Craster RV (2004) Rupture analysis of the corneal mucus layer of the tear film. *Mol Simul* 30:167–72
- Zhong L, Ketelaar CF, Braun RJ, Begley CG, King-Smith PE (2018) Mathematical modeling of glob-driven tear film breakup. *Math Med Biol* To appear, pp 1–38
- Zubkov VS, Breward CJ, Gaffney EA (2012) Coupling fluid and solute dynamics within the ocular surface tear film: a modelling study of black line osmolarity. *Bull Math Biol* 74:2062–2093
- Zubkov VS, Breward CJW, Gaffney EA (2013) Meniscal tear film fluid dynamics near Marx's line. *Bull Math Biol* 75(9):1524–1543